PHYSICAL REVIEW B **107**, 205417 (2023)

Effects of random alloy disorder, shape deformation, and substrate misorientation on the exciton lifetime and fine structure splitting of GaAs/Al$_x$Ga$_{1-x}$As(111) quantum dots

Geoffrey Pirard,[1,2,*] Francesco Basso Basset,[3] Sergio Bietti,[4] Stefano Sanguinetti,[4,5]
Rinaldo Trotta,[3] and Gabriel Bester[1,2,†]
[1]Physical Chemistry and Physics Departments, Universität Hamburg, HARBOR, Building 610,
Luruper Chaussee 149, D-22761 Hamburg, Germany
[2]The Hamburg Centre for Ultrafast Imaging, Universität Hamburg, Luruper Chaussee 149, D-22761 Hamburg, Germany
[3]Dipartimento di Fisica, Sapienza Università di Roma, Piazzale A. Moro 5, I-00185, Roma, Italy
[4]L-NESS and Dipartimento di Scienza dei Materiali, Università degli Studi di Milano-Bicocca, Via Cozzi 55, I-20125 Milano, Italy
[5]L-NESS and CNR-IFN, Piazza Leonardo da Vinci 32, Milano, Italy

(Received 24 August 2022; revised 4 March 2023; accepted 3 April 2023; published 24 May 2023)

Using atomistic, million-atom screened pseudopotential theory together with configuration interaction, as well as atomically resolved structures based on experimental characterization, we perform numerical calculations on self-assembled GaAs/Al$_x$Ga$_{1-x}$As(111) quantum dots that we compare with our experimental data. We show that random alloy disorder in the barrier can cause a symmetry breaking at the single-particle level (distortions of wave functions and lifting of degeneracies) which translates into the appearance of a nonzero exciton fine structure splitting (FSS) at the many-body level. Nevertheless, our results indicate that varying the concentration of aluminum in the random alloyed barrier allows simultaneous tuning of the exciton fine structure splitting and emission wavelength without altering its radiative lifetime $\tau \approx 200$ ps. Additionally, the optical properties of these quantum dots are predicted to be very robust against both symmetric and asymmetric shape elongation (with FSS $\leqslant 2.2$ μeV), rendering postselection less essential under well-controlled growth conditions. On the other hand, the growth on miscut substrates introduces a structural anisotropy along the quantization axis to which the system is very sensitive: the FSS ranges between 5 and 50 μeV while the radiative lifetime of the transition is increased up to $\tau = 400$ ps. The numerical results for the FSS are in perfect agreement with our experimental measurements which give FSS $= 10 \pm 9$ μeV for 2° miscut angle at $x = 0.15$.

DOI: 10.1103/PhysRevB.107.205417

I. INTRODUCTION

Self-assembled quantum dots (QDs) represent promising solid-state quantum emitters for quantum information processing applications [1]. Their potential to generate pairs of polarized-entangled photons has been at the heart of many studies since the biexciton-exciton ground-state cascade was discovered [2] and progress in this area was recently reviewed both from a general perspective [3–5] and by considering applications in quantum information technology [6–8]. Owing to the intrinsic C_{3v} symmetry inherent to III-V semiconductor nanostructures grown along the [111] crystal axis, suppression of the fine structure splitting (FSS) between the two bright exciton states can be achieved in such systems. As a matter of fact, shortly after a vanishing FSS was theoretically predicted for QDs grown along the [111] direction [9], many promising results were reported by several experimental groups [10–12]. Such achievements were made possible by the emergence of droplet epitaxy techniques [13,14] which allow, in principle, to grow perfectly symmetric strain-free structures on (111) surfaces. In practice, however, optimal growth parameters are still under investigation [15,16] and one must often resort to postselection, rendering large-scale implementation unattainable. Moreover, it has been pointed out that future integration of GaAs/Al$_x$Ga$_{1-x}$As(111) QDs into photonic heterostructures could require the use of misoriented substrates for their growth [17]. However, this procedure generates steps altering the base of the quantum dots, which can affect their optical properties and possibly be detrimental for potential applications.

This paper is intended to address these issues by considering the influence of frequently observed fabrication-related perturbations on the optical properties of GaAs/Al$_x$Ga$_{1-x}$As(111) QDs grown by droplet epitaxy on GaAs (111)A substrates. This study will be conducted for the most part from a theoretical perspective and the numerical results will be confronted with their experimental counterparts insofar as sufficient data are available. To this purpose, information about the samples' fabrication and characterization is given in Appendix A. Then, after presenting our model in Sec. II (the complete numerical

---

[*] geoffrey.pirard@chemie.uni-hamburg.de

[†] gabriel.bester@uni-hamburg.de

TABLE I. Ensembles of GaAs/Al$_x$Ga$_{1-x}$As(111) QDs used for the calculations. d, h, d_s, and d_a are, respectively, the diameter, the height, and the symmetric and the asymmetric deformations of the QD. x is the Al content in the barrier material while α is the angle of miscut. More details are given in the main text.

Series	d (nm)	h (nm)	x	d_s (%)	d_a (%)	α (Deg)
S1	70	4	0.05 to 1	0	0	0
S2	70	4	0.15	0 to 1	0	0
S3	70	4	0.15 and 1	0	0 to 1	0
S4	70	4	0.15 and 1	0	0 and 0.25	0 to 3

methodology is detailed in Appendix B), we provide in Sec. III A an analysis of the electronic structure of such QDs at the single-particle level. The next sections in Sec. III B are dedicated to the study of the FSS and the radiative lifetime and their evolution under the influence of alloy disorder and structural deformations. In particular, we focus on their variations against (i) different random alloy compositions and distributions, (ii) both symmetric and asymmetric in-plane shape elongations, and (iii) base anisotropy (due to growth on miscut structures). Finally, we sum up our main findings in Sec. IV.

II. MODEL

The atomistic architecture of the systems examined here is inspired by the work of Jo *et al.* [15] who have shown that the GaAs/Al$_x$Ga$_{1-x}$As(111) QDs take the form of truncated pyramidal nanostructures whose base shape can range from hexagonal to triangular. The prototype QD for this study is taken from the experimental work performed by Basso Basset *et al.* [18] and it is an hexagonal-based GaAs/Al$_{0.15}$Ga$_{0.85}$As(111) QD with a diameter d equal to 70 nm and a height $h = 4$ nm. Note that the QD diameter is defined as the maximum lateral dimension of the base. The S1 series in Table I represents the ensemble of QDs used to investigate the effects of an alteration of the random alloy composition on the QD properties. Moreover, it was pointed out that, by controlling the Ga adatom incorporation during the arsenization, it is possible to obtain nanostructures with different shapes gradually spanning from hexagonal to triangular. Indeed, the Ga adatom incorporation on facets $(11\bar{2})$ and $(\bar{1}\bar{1}2)$ can be regulated by changing the substrate temperature [15] or the beam equivalent pressure of the As flux [19]. This diversity in the base shape is treated in this study by adding symmetric (in-plane) deformations to the QD base, as indicated by the S2 series in Table I. A visual representation of the shape irregularity d_s is provided at the top of Fig. 4: for d_s= 0%, the shape of the base is a regular hexagon while for d_s= 100% it becomes an equilateral triangle; in-between, it consists of an irregular hexagon for which the length of the sides scales linearly with d_s. Besides, we also take into account the possible occurrence of asymmetric deformations on one (S3 series) or two (S4 series) sides of the QD that can result from faster growth in a specific direction due to anisotropic diffusion. In Figs. 2 and 5, the geometrical meaning of the quantity d_a is depicted. Finally, we investigate the consequences of using miscut substrates during the fabrication process; in this case, it was shown [16] that the elongation happens to be oriented along the terraces following the $[1\bar{1}0]$ crystal axis when the miscut follows the $[11\bar{2}]$ direction. A profile image of the miscut structure is displayed in the inset of Fig. 6(b) in order to clarify the meaning of the miscut angle α and how it is related to the steps created at the bottom of the QDs.

III. RESULTS

A. Single-particle physics

In this first section, we present the single-particle wave functions for the hexagonal-based QDs (i) embedded in a matrix of AlAs, (ii) surrounded by an alloyed barrier with 15% aluminum content, and (iii) in the presence of a base elongation d_a and a miscut angle α.

1. AlAs barrier case: Ideal C_{3v} symmetry

In the case of the GaAs/AlAs(111) QD, the wave functions are perfectly symmetric, which constitutes the expected result for a quantum dot with C_{3v} symmetry. The first five conduction states (labeled e_0, e_1, e_2, e_3, e_4) are displayed in Figs. 1(a)–1(e). The corresponding energy diagram shows one *s-like* state followed by two degenerate *p-like* states and two degenerate *d-like* states. The first five valence states, labeled h_0, h_1, h_2, h_3, h_4, are not degenerate but the hole and electron probabilities of density are almost identical: their in-plane spread is almost the same while in the quantization direction [111] (not shown) the electrons occupy slightly more space. The two types of carriers are also well localized within the boundaries of the quantum dot.

It is interesting to compare the structure of the eigenstates obtained from the atomistic empirical pseudopotential method (EPM) and their energy spectrum with the Fock-Darwin states [20,21], which constitute the solution of Schrödinger's equation for the two-dimensional quantum harmonic oscillator. In this effective mass treatment, the eigenfunctions are given in polar coordinates by [22]

$$\psi_{n_r,l}(r,\phi) = \frac{\beta}{\sqrt{2\pi}}\sqrt{\frac{n_r!}{(n_r+|l|)!}}e^{-\frac{\beta^2r^2}{4}}e^{il\phi}\left(\frac{\beta r}{\sqrt{2}}\right)^{|l|} \times L_{n_r}^{|l|}\left(\frac{\beta^2r^2}{2}\right), \tag{1}$$

where n_r and l are, respectively, the radial and azimuthal quantum numbers. $\beta = \sqrt{m\omega/\hbar}$ is a constant for a given material, m being its effective mass while ω is the oscillator frequency. The $L_{n_r}^{|l|}(\cdot)$ functions are generalized Laguerre polynomials. The corresponding energies are given by

$$E_{2D}(n_r, l) = (2n_r + |l| + 1)\hbar\omega. \tag{2}$$

It turns out that all the states of the GaAs/AlAs QD can be approximated quite accurately by this simplified model. Since the confinement potential is not cylindrical but hexagonal, one of the main differences is that all the conduction states have the C_{6v} (hexagonal) symmetry while for all the valence states the C_{3v} atomistic symmetry of the nanostructure is preserved (see Appendix C for more details). Besides, some degeneracies are the same as those of the Fock-Darwin states

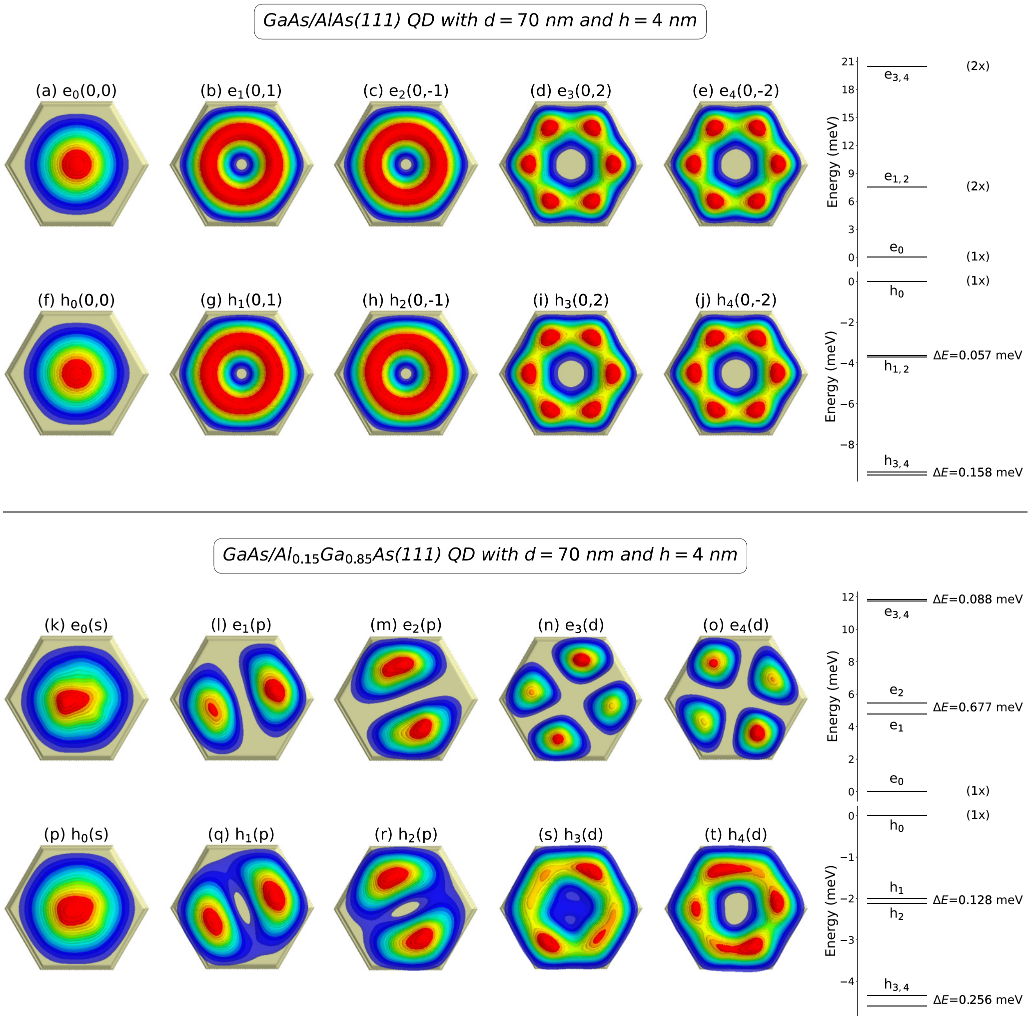

FIG. 1. Cross sections in the (111) plane of the single-particle electron and hole-squared wave functions for the GaAs/AlAs QD (top panel) and a GaAs/$\mathrm{Al}_{0.15}\mathrm{Ga}_{0.85}$As QD (bottom panel). The conduction states are denoted e_0, e_1, e_2, e_3, e_4. An energy diagram provides the energy splittings between the states and the reference is taken at the bottom of the conduction band (e_0). Similarly, the valence states are labeled h_0, h_1, h_2, h_3, h_4 and the reference energy is set at the top of the valence band (h_0). When two states have the same energy, their degeneracy is given on the right of the diagram while for two states with a small energy splitting ΔE, the numerical value of the splitting is provided. These energy splittings between the states are also provided in Figs. 8–11 for all the wave functions relevant to this study. In the case of GaAs/AlAs QD, the states are labeled using the Fock-Darwin notation [20–22] (n_r, l) to emphasize the similarity with this simple model. On the other hand, for GaAs/$\mathrm{Al}_{0.15}\mathrm{Ga}_{0.85}$As QD, the symmetry of each state, given between parentheses, is inspired from the atomic notation (s, p, d). All the wave-function plots presented in this paper were generated using a python script based on the MAYAVI2 package [23]. The diameter and the height of the quantum dots are, respectively, equal to 70 and 4 nm as given in Table I. The broken symmetry induced by the random alloy for the GaAs/$\mathrm{Al}_{0.15}\mathrm{Ga}_{0.85}$As QD clearly manifests in the wave functions as compared to the highly symmetric nature of the GaAs/AlAs QD states.

[e.g., for the conduction $(0, \pm 1)$ and $(0, \pm 2)$ states] while others are lifted owing to the actual symmetry of the system. Additional information is given in Appendix C in Figs. 8 and 9 where all the 18 conduction and valence wave functions are plotted.

Note that we have labeled the states using the Fock-Darwin notation (n_r, l) to emphasize the similarity between the atomistic EPM results and this well-known analytical toy model. It is only meant to provide an intuitive picture to the reader who should keep in mind that all the calculations in this work have been performed within the EPM+SLCBB framework. Indeed, Eq. (2) supposes that nondegenerate energy levels are equally spaced (by steps of $\hbar\omega$), an assumption in striking contrast to our numerical results (see Appendix C for a more comprehensive discussion).

2. *Perturbation by a random alloy: $\mathrm{Al}_{0.15}\mathrm{Ga}_{0.85}$As barrier*

When the barrier material AlAs is replaced with a random alloy (in the present case $\mathrm{Al}_{0.15}\mathrm{Ga}_{0.85}$As), the C_{3v} symmetry is broken, as can be seen in Figs. 1(k)–1(t). For both the conduction and valence states, the *s-like* ground state is slightly deformed owing to the irregular distribution of the atoms surrounding the dot; besides, a significant spread of the wave functions is observed: the density of probability outside the boundaries of the QDs has now a finite value. The random

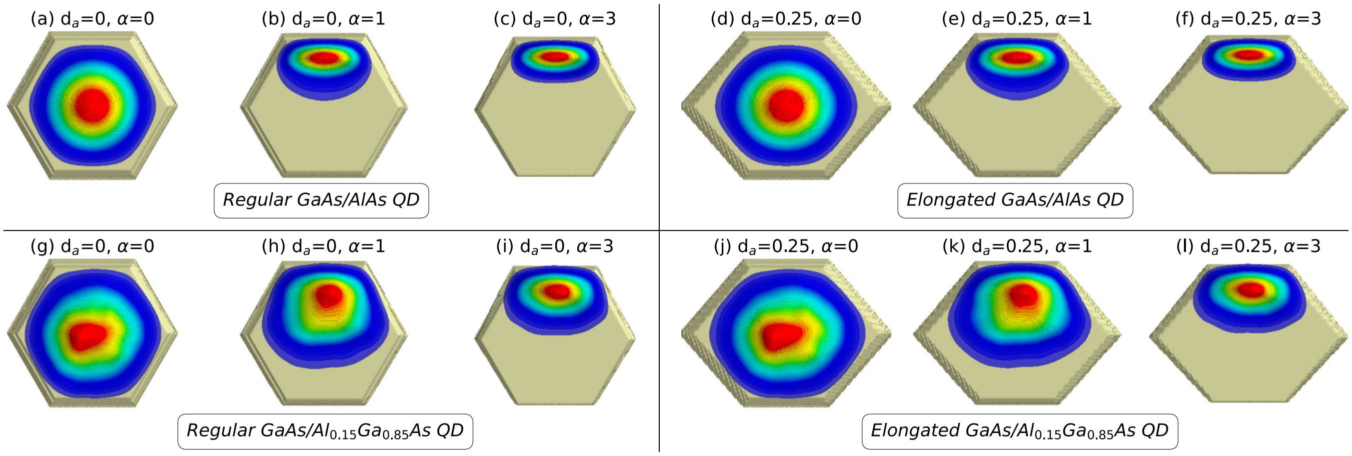

FIG. 2. Cross sections in the (111) plane of the single-particle electron ground-state wave functions (e_0) for AlAs barrier (top) and $Al_{0.15}Ga_{0.85}As$ matrix (bottom). Their evolution with respect to an increasing miscut angle ($\alpha \in \{0^\circ, 1^\circ, 3^\circ\}$) is depicted for QDs with regular (a)–(c) and (g)–(i) and elongated (d)–(f) and (j)–(l) bases. The terraces and the elongation are both aligned (horizontally) with the $[1\bar{1}0]$ crystal direction. In all cases where $\alpha \neq 0$, the wave function tends to localize within the first few steps, with a stronger confinement for GaAs/AlAs QDs than for GaAs/$Al_{0.15}Ga_{0.85}$As QDs.

alloy introduces the same preferential orientation for the first *s-like* states (e_0, h_0) and the first *p-like* states (e_1, h_1) while the second *p-like* states (e_2, h_2) are oriented perpendicularly to this direction. Additional calculations not presented in this paper show that this observation is valid for different realizations of the random alloy (with a different preferential direction for each distribution considered). Finally, the degeneracy of the *p-like* and *d-like* conduction states is lifted and the splittings between states of same pseudo-orbital angular momentum are enhanced. On the other hand, the energy splittings between *s-like* and *p-like* or *p-like* and *d-like* states are reduced due to a weaker confinement potential (relative to the $x = 1.00$ case). Further analysis including all the 18 calculated conduction and valence states for $x = 0.15$ is proposed in Appendix C (see Figs. 10 and 11).

In the following sections, we will see how the small distortions and energy splittings presented above are sufficient to induce observable consequences on the optical properties of the quantum dots.

3. Influence of elongation and miscut

The growth on miscut structures is often accompanied with an elongation of the quantum dots. In Fig. 2, the electronic ground-state wave functions (e_0) are compared for $d_a = \{0.00, 0.25\}$, $\alpha = \{1^\circ, 2^\circ, 3^\circ\}$, and $x = \{0.15, 1.00\}$. Interestingly, despite an expected lift of degeneracy, the symmetry of the wave functions for elongated quantum dots is close to the ideal case [see Fig. 2(a) vs Fig. 2(d) and Fig. 2(g) vs Fig. 2(j)]. Base elongation allows nonetheless a bigger extension of the carriers' wave functions. On the other hand, the presence of a miscut angle is responsible for creating steps affecting the base of the QDs. In other words, the height of the quantum dot now varies along the $[11\bar{2}]$ crystal axis (vertical direction), forcing the carriers to preferentially localize where the height is the largest, i.e., on the top of the structures. Figures 2(b) and 2(c), 2(e) and 2(f), 2(h) and 2(i), and 2(k) and 2(l) show that increasing the miscut angle strengthens the localization of the electrons. The hole density follows the same pattern (not shown). It must be noted that the carriers are mostly confined inside a single step for AlAs ($x = 1.00$) while they are able to spread over two or more steps when $x = 0.15$. Therefore, we can anticipate that the overlap between the electron and hole wave functions will lead to more drastic changes in the optical properties of these quantum dots, with a noticeable difference between strongly confined ($x = 1.00$) and weakly confined ($x = 0.15$) states.

B. Influence of internal perturbations on the optical properties of GaAs/AlGaAs(111) QDs

Several types of in-built defects created during the QDs fabrication can affect their optical properties. The rest of this paper focuses on several kinds of perturbations and their consequences on the photoluminescence (PL) emission including FSS and radiative lifetime of the bright exciton doublet. Particular attention is given to (i) the composition x of the random alloy barrier and its fluctuations, (ii) the symmetric deformation of the base d_s, (iii) the asymmetric elongation of the base d_a, and (iv) the growth on miscut substrates with an angle α along $[11\bar{2}]$.

1. Composition and fluctuations of the $Al_xGa_{1-x}As$ random alloyed barrier

Even for QDs sharing the same nominal symmetry, the random alloy composition and fluctuations can perturb the atomistic structure, leading to observable consequences on the single-particle physics (see Sec. III A 2). We examine now the excitonic properties and find out that nonzero FSS values emerge. In order to probe the response of the system to the disorder induced by the barrier material at the many-body scale, the FSS is averaged here over six different random alloy distributions for each point considered in Fig. 3, i.e., for every barrier composition x. Indeed, for a quantity as small and sensitive as the FSS, the way the atoms are arranged in the surrounding matrix, even for the same

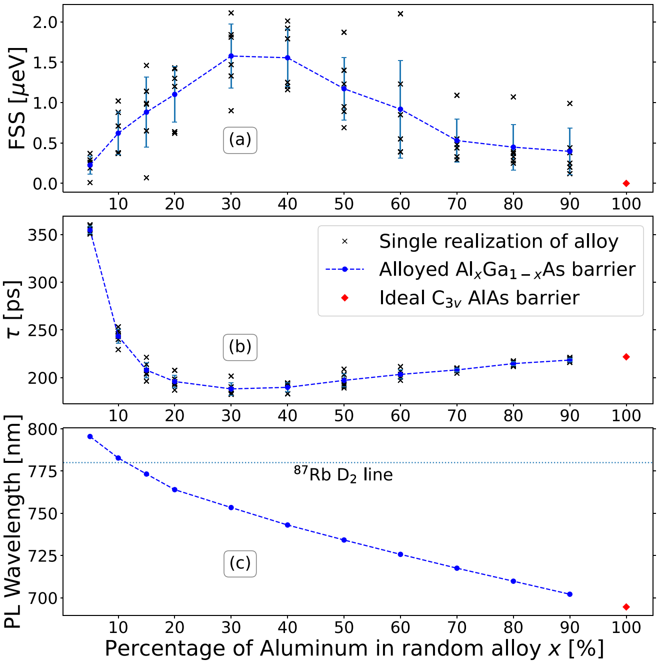

FIG. 3. Evolution of the exciton fine structure splitting (a), the radiative lifetime (b), and the PL emission (c) as a function of the percentage of aluminum x in the random alloy. Each single realization of the alloyed matrix is represented by a black cross while the average and standard deviation for each value of x appear, respectively, as blue circles and blue error bars. The pure AlAs alloy ($x = 1.00$) is symbolized as a red diamond.

aluminum content, can lead to a significant standard deviation that bears physical relevance when considering the feasibility of polarized-entangled photons emitters.

In Fig. 3(a) the FSS as a function of the fraction of aluminum in the barrier material x is plotted. A bell-shaped curve is apparent but it is not centered around 50% where the disorder is expected to be maximized. In fact, the maximum FSS is obtained when the concentration of aluminum in the alloy approaches 30%–40% but, given the high standard deviation, the occurrence of the maximum at $x \neq 0.50$ could be due simply to the small number of random alloy realizations considered here for each value of x. The FSS decreases to exactly zero when the aluminum concentration is equal to 100%, i.e., when there is no randomness anymore as the C_{3v} symmetry is restored. This agrees well with the corresponding wave functions presented before and the general predictions of group theory. Interestingly, the fine structure splitting also decreases when the Al concentration gets closer to 0% (limiting case where the confinement is totally lost) and drops below 1 μeV for $x \leqslant 15\%$. Hence, the FSS should be minimal and useful for the generation of entangled-photon pairs if experiments are performed on GaAs(111) QDs surrounded by a barrier material containing less than 15% of aluminum. A good compromise in the present case is $x = 10\%$ as the carriers' wave functions start to leak outside the QDs considerably when the concentration of aluminum becomes smaller. For quantum information technology applications, the PL emission also plays an important role when designing quantum structures. It is indeed desirable, in the context of quantum memory implementation, to generate entangled photons which will be emitted in resonance with the D_2 line of rubidium atoms (780 nm) [24–28]. Interestingly, as can been seen in Fig. 3(c), it turns out that by lowering the concentration of aluminum below 15%, the desired wavelength for applications in quantum memories can be achieved. Our numerical results predict that, for the geometry we have considered, growing GaAs/Al$_{0.10}$Ga$_{0.90}$As(111) QDs can match both requirements. We then recommend from this perspective the use of a low aluminum concentration in the AlGaAs matrix for quantum information applications. From an experimental viewpoint, if one wants to avoid reducing too much the confinement, they can also achieve the desired emission energy by using a smaller QD size, but a symmetric and defect-free shape might become harder to obtain, which results in a compromise between the two parameters.

Finally, Fig. 3(b) shows the evolution of the bright exciton radiative lifetime as a function of x. The concentration of aluminum does not seem to significantly affect the average lifetime which remains almost constant and close to 200 ps, except when the confinement potential becomes very weak at $x < 0.10$.

2. Symmetric variation of the QD base: From regular hexagon to equilateral triangle

As discussed in Sec. II, the base of the QD may come in different shapes depending on the crystallization temperature. Here, we investigate whether a symmetric transition from a regular hexagon to an equilateral triangle (series S4 in Table I) bears any major consequences on the optics. For this study and in the following, averaging over several points is computationally demanding and less relevant: therefore, only one particular alloy distribution at $x = 15\%$ is selected for which FSS = 1.46 μeV at $d_s = 0\%$. Note that, far from the QDs, the alloy distribution is always the same. Since the diameter and the height of the QDs are kept constant, some deviations can exist near the QD/barrier interface, due to the alteration of the QD base (as the volume occupied by the QDs for different d_s, d_a and α is not exactly the same). Nevertheless, for $d_s \neq 0$ and $d_a \neq 0$, these small differences occur far from the QDs center where the wave function reacts more strongly to the alloy distribution. For $\alpha \neq 0$, this effect is also negligible because the localization of the carriers induced by the miscut steps is the dominant effect.

The fine structure splitting variation with respect to a symmetric deformation of the QD base varies from 1 to 1.5 μeV, as can be seen in Fig. 4(a). It is the highest for 0% and 100% deformation of the base, which corresponds to regular hexagon and equilateral triangle, respectively; it drops in-between for irregular hexagonal bases. Nevertheless, the range of values is narrow relative to the variance at $d_s = 0\%$ and will fall within the uncertainty induced by the fluctuations of the random alloy. Indeed, in spite of the fact that the specific random alloy realization chosen for this study is the one maximizing the FSS at $d_s = 0\%$, most of the points remain inside the limits of the error bars. Thus, we come to the conclusion that the influence of a shape irregularity has only a negligible effect on the magnitude of the FSS, as long as the system retains its nominal C_{3v} symmetry. This finding constitutes an

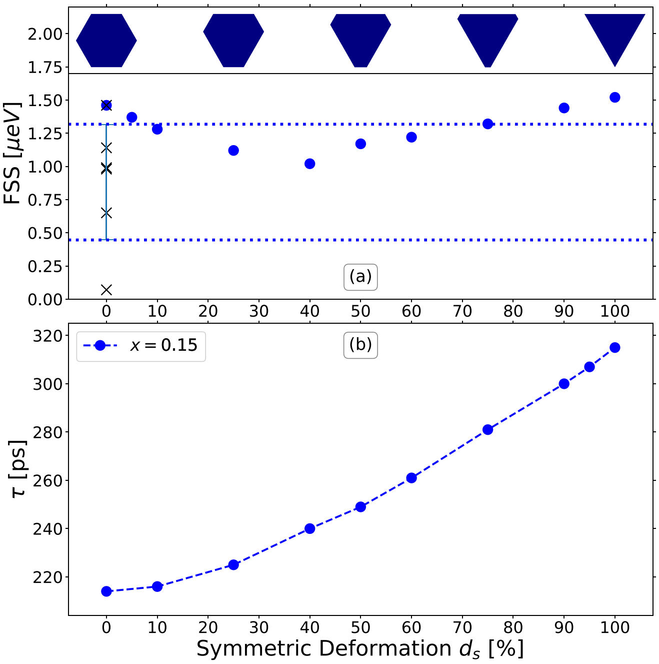

FIG. 4. FSS (a) and τ (b) vs symmetric deformation d_s. The deformation happens on three sides: 0% corresponds to the regular hexagon and 100% is triangular. Intermediate cases are irregular hexagons which respect the nominal C_{3v} symmetry. The data points (black crosses) and the standard deviation (dotted lines) from Fig. 3(a) at $x = 0.15$ are reproduced in Fig. 4(a) for comparison. The top of the figure represents different shapes of the QD base. The diameter and the height are kept constant ($d = 70$ nm and $h = 4$ nm).

important result as it points out that a precise control of the base shape is not paramount to minimize the FSS and achieve entangled-polarized photon pair emission.

On the contrary, the radiative lifetime τ grows monotonically when d_s is increased [see Fig. 4(b)]. This result demonstrates that when the base is an equilateral triangle, the lifetime can exceed 300 ps while it reaches only 200 ps for the hexagonal-based QDs. Note, however, that the QD diameter is kept constant but not its volume that the holes and electrons can occupy differently for each amplitude of deformation. Hence, the observed behavior can be attributed to a weaker overlap between the carriers' wave functions when $d_s = 100\%$.

3. Robustness of the optical properties of QDs with a shape asymmetry: Base elongation

Large GaAs/AlGaAs(111) droplet epitaxial QDs can develop faster in one specific direction, giving rise to a base elongation which may, in principle, completely break the C_{3v} symmetry. One could therefore presume that even a tiny shape asymmetry could lead to a visible elevation of the fine structure splitting. In fact, this increase is remarkably small: for $d_a = 5\%$, $\Delta\text{FSS} = 0.35$ µeV for both $x = 0.15$ and 1.00 as depicted in Fig. 5. Thus, for the QDs considered here, the presence of a random alloyed barrier is actually much more relevant to the optical properties than the existence of a small elongation. The two curves in Fig. 5 follow a linear progression up to $d_a = 25\%$ (with different slopes) until they start converging for $d_a \geqslant 60\%$. It turns out that for very large deformations, the influence of the random alloy becomes negligible relative to d_a. But the FSS never exceeds 2.5 µeV, a particularly low limit given the drastic deformation applied to the QD. The minor impact of in-plane elongation on the FSS can be explained by the big size of the QD base which attenuates quantum confinement effects, so that the system does not strongly react to in-plane symmetry breaking. Furthermore, the inset of Fig. 5 indicates that the lifetime is also barely affected by the anisotropic deformation of the base. From this analysis, we can conclude that truncated pyramidal quantum dots with an hexagonal base grown on (111) surfaces are extremely robust against shape asymmetry. During the growth of an ensemble of quantum dots, the most imperfect ones should then not have a tremendous influence on the quality of the optical properties, rendering postselection based on the shape asymmetry of the QD less critical.

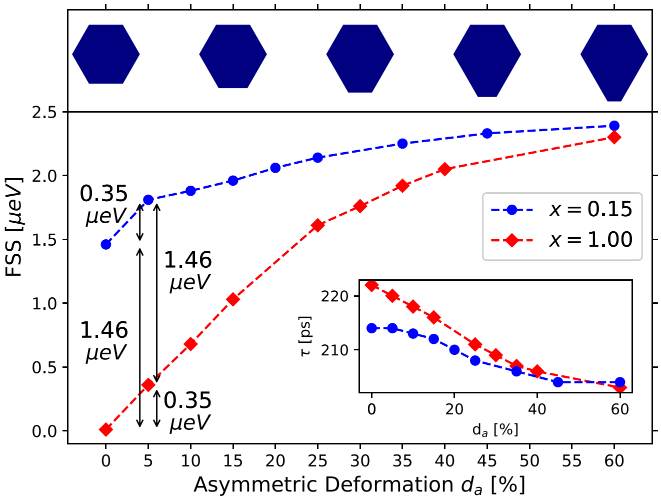

FIG. 5. FSS vs asymmetric deformation d_a. The elongation happens on one side only: $[11\bar{2}]$. A pictorial representation of the base shape is given on top of the plot for several values of elongation. The proportion of aluminum in the random alloy $Al_xGa_{1-x}As$ is given as x. The height is kept constant ($h = 4$ nm) while the length of the base is allowed to vary only along the direction of the elongation. Inset: plot of τ vs d_a.

4. Change of optical properties for QDs with a structural asymmetry due to a growth on miscut surfaces

Contrary to the case of in-plane elongation, the symmetry-breaking generated by growing QDs on misoriented substrates is very pronounced as it impacts the quantization axis of the nanostructure. Owing to the formation of steps, the height of the system becomes dependent on the $X = [1\bar{1}0]$ and $Y = [11\bar{2}]$ coordinates so that quantum confinement effects are expected to considerably influence the optical properties of the QDs. For this reason, two distinct aluminum concentrations ($x = 0.15$ and 1.00) will again be considered. Besides, since the presence of a miscut surface generally provokes an in-plane elongation for large QDs [16], this contribution will be singled out by comparing the two cases $d_a = 0\%$ and 25%.

The FSS, the radiative lifetime and the degree of linear polarization (DLP) of the QDs from series S4 in Table I are

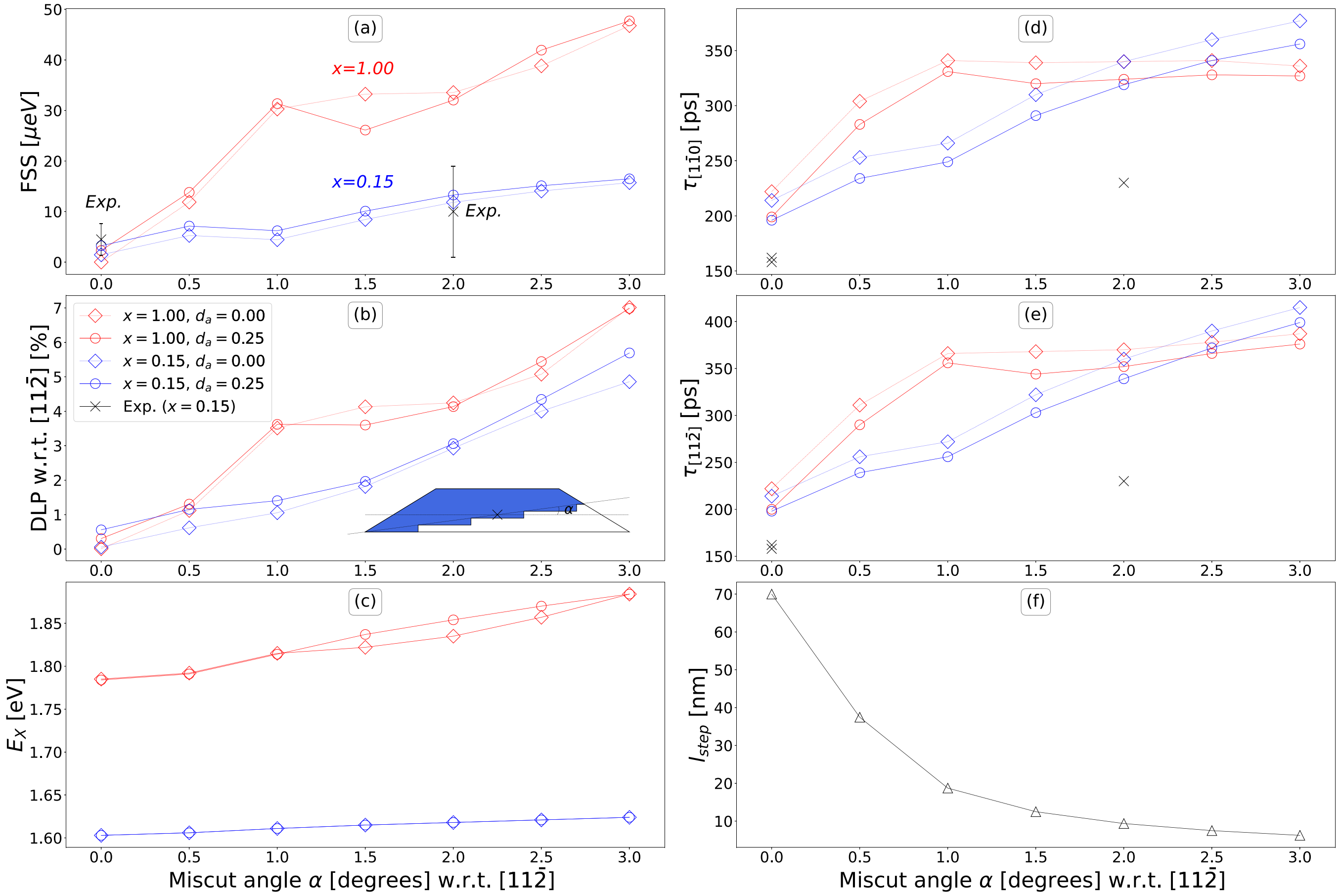

FIG. 6. Exciton fine structure splitting (a), degree of linear polarization (b), emission energy (c), and radiative lifetime (d), (e) for regular (dotted lines) and elongated (solid lines) QDs and length of the steps introduced by the miscut (f) vs miscut angle α. The blue color corresponds to $x = 0.15$ (alloyed barrier) while the red color represents QDs with nonalloyed barrier. A schematic view of the miscut QDs is provided in the inset of (b). The DLP is plotted with respect to $[11\bar{2}]$ rather than in absolute value, i.e., it is defined as $(I_{[1\bar{1}0]} - I_{[11\bar{2}]})/(I_{[1\bar{1}0]} + I_{[11\bar{2}]})$, a choice justified by the orthogonal polarizations of the two bright exciton states and useful for its comparison with the contrast in lifetime in Fig. 7.

plotted as a function of the miscut angle α in Fig. 6. We observe that all these quantities are strongly amplified when the value of the miscut angle increases. Let us have a closer look at this behavior quantitatively by separating the effects of alloy randomness and base deformation, starting with the FSS. First, we consider the QDs surrounded by an alloyed barrier with 15% of aluminum content [described by the blue points in Fig. 6(a)]. The addition of elongation raises the value of the FSS from 1.46 to 3.25 μeV at $\alpha = 0°$ and shifts the corresponding plots by a quasiconstant amount of about 1.7 μeV when $\alpha \neq 0°$. This value is almost independent of x and α and consistent with the results of Sec. III B 3 (although the elongation occurs here in another direction). Note that we expect the nonalloyed QDs to share the same qualitative behavior with respect to the base elongation, but with a much steeper slope due to stronger confinement for $x = 1.00$ (bringing the electron and the hole closer to each other, hence enhancing the value of the electron-hole exchange matrix elements). The apparent anomalies ($\alpha = 1.5°$, $\alpha = 2°$, $\alpha = 2.5°$) come from a slightly different design in the geometry of these QDs. Nonetheless, these fluctuations of the FSS with respect to the exact atomic arrangement of the terraces are consistent with what we observe in our experiments. There exists indeed a large standard deviation in the experimental data [represented by the black error bars in Fig. 6(a)] which is due to a naturally large dispersion that we attribute to the potentially large variance in the position of the atomic terraces with respect to the base of the quantum dot. Furthermore, our numerical results are in excellent agreement with our measurements performed for $\alpha = 0°$ and 2° (at $x = 0.15$) which give FSS($\alpha = 0°$) = 4.5 ± 3.1 μeV and FSS($\alpha = 2°$) = 10 ± 9 μeV as reported in Fig. 6(a) by the black points (the average and the standard deviation are estimated over a sample size of 29 and 32 QDs, respectively). Both our regular [FSS($\alpha = 0°$) = 1.46 μeV, FSS($\alpha = 2°$) = 11.84 μeV] and elongated [FSS($\alpha = 0°$) = 3.25 μeV, FSS($\alpha = 2°$) = 13.28 μeV] QDs calculated points fall within the experimental standard deviations and are reasonably close to the measured averages. Indeed, there exists a small difference between the numerical and experimental averages, but it should be also accounted in this comparison that the real angle of miscut of the substrates can deviate from the nominal value by ±0.5°. Hence, the substantial robustness of GaAs/$\mathrm{Al}_x\mathrm{Ga}_{1-x}\mathrm{As}(111)$ QD properties against in-plane shape anisotropy discovered in the previous section is confirmed for $[1\bar{1}0]$-elongated QDs, whereas the miscut angle carries more serious consequences. These findings are interesting from an experimental point of view as they indicate that unwanted deformations occurring during QD growth do not significantly degrade their optical properties while the boost in the FSS caused by the miscut angle can be controlled during the fabrication process. Moreover, for small x, the FSS only grows by a negligible amount between $\alpha = 2^\circ$ and 3°. Thus, for an optimal control over the miscut QD properties, it is advisable to use intermediate values of α. They are also more easily accessible since the experimental uncertainty on the miscut angle is equal to $\Delta\alpha = \pm 0.5^\circ$, so that the use of $\alpha < 1^\circ$ can lead to poor reproducibility. In order to minimize the FSS for bigger α, we predict, based on our previous findings in Sec. III B 1, that the choice of $x = 0.10$ should again constitute a good alternative as we anticipate the slope of the curve to be flatter.

In addition, we note that our QD ensembles for both $\alpha = 0^\circ$ and 2° emit in a narrow range of energy $\Delta E(X)_{\text{expt}} = 1.58$–$1.61$ eV, making miscut QDs suitable to emit at a desired energy. This interval is also calculated, and we get $\Delta E(X)_{th} = 1.603$–1.618 eV. The predicted trend is linear for both regular and elongated QDs [see Fig. 6(c)] but the slope is too small to be noticed experimentally due to the heterogeneity of the samples. More precisely, the size dispersion characteristic of the growth technique is larger than the difference observed by increasing the miscut angle with the $x = 0.15$ barrier. Note that the linear trend implies that the FSS as well as the DLP and the lifetime (discussed below) will possess the same dependence with the emission energy E_X as they have with α. This observation should remain valid for $x = 1.00$ if the anomalies are not considered. Since only two values of x have been considered in this work, it is not possible to conclude that this behavior is transferable to any random alloy composition. It could nonetheless constitute a plausible generalization and a hypothesis to investigate further in future research.

Another interesting feature that emerges from the study of miscut QDs is the appearance of two distinct polarized excitonic states $X_{[1\bar{1}0]}$ and $X_{[11\bar{2}]}$, where the $|X_{[1\bar{1}0]}\rangle \rightarrow |\Phi_0\rangle$ transition is energetically lower. This results in a net total polarization of the emission for $\alpha > 0^\circ$ which is highlighted in Fig. 6(b) by the nonzero values of the DLP for both $x = 0.15$ and 1.00. Nevertheless, the DLP only increases by a few percent which is comparable to the degree of polarization induced by the optical elements in the collection path. The emission observed in the experiments is compatible with an unpolarized source within such interval of confidence. In practice, the application of external strain or the use of InAs QDs can enhance the value of the DLP and provide a test to substantiate these numerical predictions [29]. Size effects could also play an important role as linear polarization values up to 50% were recently reported [30] for smaller (111)A QDs without elongation.

Finally, the exciton is now allowed to decay through two distinct channels with radiative lifetimes $\tau_{[1\bar{1}0]}$ and $\tau_{[11\bar{2}]}$, as pictured in Figs. 6(d) and 6(e). Qualitatively, the two curves are similar but $X_{[11\bar{2}]}$ possesses higher lifetime compared to $X_{[1\bar{1}0]}$ when $\alpha > 0^\circ$ because the exciton lifetime asymmetry $\Delta\tau = |\tau_{[1\bar{1}0]} - \tau_{[11\bar{2}]}|$ is enhanced by the miscut angle. For $x = 1.00$ and $\alpha = 0^\circ$, $\Delta\tau = 0$ because the two exciton bright states belong to the same irreducible representation in the C_{3v} point group. When this condition is not satisfied (e.g., for $x \neq 1.00$ or $\alpha \neq 0^\circ$), the lifetime asymmetry differs from zero [31]. Just as the FSS previously studied constitutes an important figure of merit regarding applications in quantum technologies as the main limiting factor to achieve high fidelity in polarized-entangled photon states [32,33], it has been pointed out [34] that $\Delta\tau$ provides a good measure of the symmetry of InAs/GaAs(001) QDs. We show here that this idea can in fact be extended and generalized to the case of GaAs/Al$_x$Ga$_{1-x}$As(111) QDs. Moreover, the contrast in lifetime

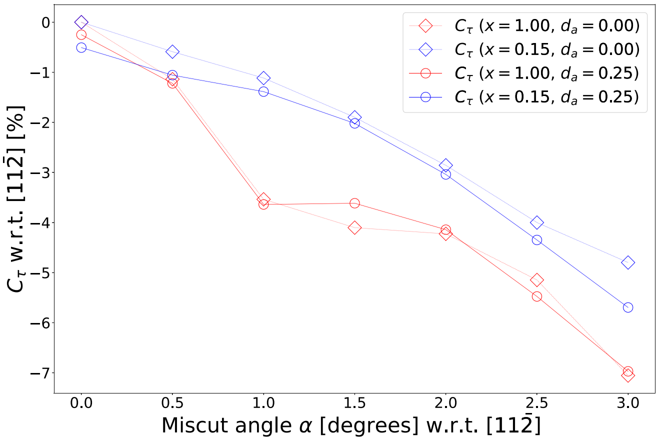

FIG. 7. Contrast in lifetime $C_\tau = (\tau_{[1\bar{1}0]} - \tau_{[11\bar{2}]})/(\tau_{[1\bar{1}0]} + \tau_{[11\bar{2}]})$ given in % vs miscut angle α. The curves exhibit exactly the same dependence on α as their counterparts in Fig. 6(b) but with a negative sign, indicating that C_τ and the DLP are closely correlated quantities.

$$C_\tau = \frac{\tau_{[1\bar{1}0]} - \tau_{[11\bar{2}]}}{\tau_{[1\bar{1}0]} + \tau_{[11\bar{2}]}} \tag{3}$$

increases monotonically to negative values with the miscut as shown in Fig. 7. It can be noted that Fig. 7 would look exactly the same as Fig. 6(b), were it not for the negative sign. This observation suggests that the DLP and the contrast C_τ should be strongly correlated quantities and indeed it is found numerically that for all x, α, and d_a,

$$||\text{DLP}(x, \alpha, d_a)| - |C_\tau(x, \alpha, d_a)|| < \epsilon, \tag{4}$$

where $\epsilon < 0.1\%$. An analytical derivation showing that $\text{DLP} = -C_\tau$ is provided in Appendix D for the case of interest, i.e., when the two exciton bright transitions have orthogonal polarizations. This condition is always fulfilled in this study and in Ref. [29] where polar diagrams have been plotted for both GaAs/Al$_x$Ga$_{1-x}$As(111) and InAs/GaAs(111) QDs.

The base elongation affects the radiative lifetime by downshifting the curve for $d_a = 0.25$ relative to $d_a = 0.00$. This effect is ascribed to the larger extension of the carriers' wave functions mentioned in Sec. III A 2. Once more, the random alloy provokes an attenuation of the slope as a consequence of weaker confinement potential. On the other hand, the different trends between $x = 0.15$ and 1.00 pose a more puzzling question. While for $x = 0.15$ $\tau_{[1\bar{1}0]}$ and $\tau_{[11\bar{2}]}$ evolve monotonically and gradually with α in a quasilinear fashion, for $x = 1.00$, a sudden increase is observed for $\alpha \leqslant 1^\circ$ which is followed by a saturation for larger angles.

In order to identify the origin of these contrasting behaviors, we need to examine in more details the geometry of miscut QDs. First of all, we remark that the volume of the QDs is not kept constant so that the electron and hole wave functions could in principle localize differently for different α, altering the overlap integrals on which the calculation of the recombination rates very much depends. However, a direct correlation between τ and the QD volume does not provide a sufficient explanation in the present case and it is actually necessary to understand how exactly the QD base is transformed across the whole range of study. If we assume only steps of one monolayer (ML) along $Z = [111]$, the number of steps n_{steps} produced by the miscut grows linearly with it for small angles [35]:

$$n_{\text{steps}} = \frac{3}{2}\frac{d}{a_0}\tan(\alpha) \approx \frac{3}{2}\frac{d}{a_0}\alpha. \tag{5}$$

On the other hand, their length l_{step} (along $Y = [11\bar{2}]$) is inversely proportional to the miscut angle according to [35]

$$l_{\text{step}} = \frac{a_0}{\sqrt{3}\tan(\alpha)} \approx \frac{a_0}{\sqrt{3}}\frac{1}{\alpha}. \tag{6}$$

By looking at Fig. 6(f), we can notice that l_{step} critically drops for $\alpha \leqslant 1^\circ$ and tends to vary more slowly for $\alpha > 1^\circ$ until it stabilizes. Now, it becomes apparent [see Figs. 2(a)–2(f)] that the single-particle carriers' wave functions try to localize within the first two steps and that the size of these first steps will determine the effective volume over which the interaction can take place. Additionally, this volume remains nearly the same for higher angles, and so does the radiative lifetime. Thus, these observations support the interpretation that the combination of l_{step} and the strong localization of the states is responsible for the behavior of τ for $x = 1.00$. In the $x = 0.15$ case, the wave functions can spread over several steps and occupy a larger volume [see Figs. 2(g)–2(l)] such that the rise in the radiative lifetime is not limited anymore and is more likely to follow a similar pattern as n_{steps} (i.e., quasilinear). These considerations complete our theoretical treatment of the radiative lifetime in miscut QDs and we eventually proceed to the last part of this study, namely, the comparison with our experiments. At $\alpha = 0^\circ$, $\tau_{\text{expt}} = \{158, 160\}$ ps while for $\alpha = 2^\circ$, $\tau_{\text{expt}} = 230$ ps. The experimental data corroborate the predicted tendency of the miscut angle to enhance the lifetime. Indeed, we find that the ratios

$$\frac{\tau_{\text{expt}}(\alpha = 0^\circ)}{\tau_{\text{expt}}(\alpha = 2^\circ)} \approx 0.7 \tag{7}$$

and

$$\frac{\tau_{th}(\alpha = 0^\circ)}{\tau_{th}(\alpha = 2^\circ)} \approx 0.6 \tag{8}$$

are in reasonable agreement given the limited set of experimental points. Nevertheless, the measured values are clearly below the ones obtained numerically. Excitons are laterally weakly confined in QDs with a large in-plane extension. As a consequence, in such nanostructures, correlation effects among the confined carriers play a major role in the description of the optical properties [36]. Now, these effects are well captured by the EPM+CI approach as long as a sufficiently large size for the CI basis is selected [37]. It is the case in this work (where an 18 × 18 basis is employed) so that the use of the CI method should not cause of any discrepancy between τ_{expt} and τ_{th}. Theoretically, another possible path to explore would be to go beyond Eqs. (B9) and (B10) in order to assess by how much τ_{th} can vary when the medium is not assumed to be homogeneous (or even local). That is to say, when the quantized vector potential operator is dependent on the dielectric function $\epsilon(\boldsymbol{r}, \boldsymbol{r}')$ in a nontrivial way and cannot be written in terms of plane waves anymore (see, e.g., Table 1 in [38]). Besides, the experimental measure could underestimate the lifetime in presence of nonradiative decay channels [39], even if those have been deemed negligible in similar emitters under resonant two-photon excitation [7]. On the other hand, the predicted simultaneous increase of the exciton FSS and lifetime with α suggests the existence of a connection between these two quantities in miscut GaAs/Al$_x$Ga$_{1-x}$As(111) QDs. Since the selected QDs for the lifetime measurements have relatively low FSS values (respectively 1.0 and 1.4 μeV for $\alpha = 0^\circ$ and 2.4 μeV for $\alpha = 2^\circ$), further experimental investigations are required to explore any possible link between FSS and exciton lifetime.

IV. CONCLUSION

In summary, we have shown that the predicted and measured FSS are in excellent agreement for GaAs/Al$_{0.15}$Ga$_{0.85}$As(111) QDs. Indeed, for $\alpha = 0^\circ$ the theoretical FSS are evaluated at 1.5 and 3.3 μeV for the regular and elongated QDs, respectively, while the experimental value is found to be 4.5 ± 3.1 μeV. Likewise, at $\alpha = 2^\circ$, the measurements estimate that the FSS is equal to 10.0 ± 9.0 μeV and the numerical results provide 11.8 and 13.3 μeV for the regular and elongated shapes, respectively.

Moreover, we have found that the FSS is exactly equal to zero for hexagonal-based GaAs/AlAs(111) QDs, in accordance with the predictions of group theory for C_{3v} systems. On the other hand, we have shown that the addition of a disordered random alloy Al$_x$Ga$_{1-x}$As causes a loss of symmetry leading to finite values of FSS. However, the magnitude of this FSS does not exceed 2 μeV, showing that this symmetry breaking can actually be leveraged: a careful choice of the aluminum composition in the barrier material allows to tune the emission spectrum, a property of great interest for wavelength-critical applications such as interfacing with quantum memories.

Besides, a deformation preserving the C_{3v} symmetry was applied to the base of the QDs (ranging from hexagonal to triangular shape), and it was proven to have only a negligible impact on the QDs optical properties. It was also demonstrated that both the radiative lifetime and the FSS are very robust against in-plane elongation, making GaAs/Al$_x$Ga$_{1-x}$As(111) QDs promising candidates for the generation of polarized-entangled photon pairs without heavily relying on QDs postselection. As a comparison, a FSS of 1 μeV with a lifetime of 200 ps would result in a decrease in fidelity of approximately 2 percentage points compared to the zero FSS case, which is comparable to the typical impact of the other parameters lowering the degree of entanglement in current state-of-the-art devices [6].

In contrast, when the growth is carried out on misoriented substrates, a substantial augmentation of both the FSS and the lifetime was demonstrated, with a slope that strongly depends on the random alloy composition. In particular, for low aluminum fraction ($x = 0.15$), the FSS remains sufficiently low so that it can be readily compensated by external tuning strategies [26]. Overall, our findings are very encouraging to push forward the study of such nanostructures.

ACKNOWLEDGMENTS

G.P., S.B., S.S., and G.B. acknowledge funding from the European Union's Horizon 2020 Research and Innovation Programme under the Marie Skłodowska-Curie ITN project 4PHOTON (Grant Agreement No. 721394). F.B.B. and R.T. acknowledge funding from the European Research Council (ERC) under the European Union's Horizon 2020 Research and Innovation Programme (SPQRel, Grant Agreement No. 679183) and by the European Union's Horizon 2020 Research and Innovation Program under Grant Agreement No. 899814 (Qurope); the research has received financial support from ICSC – Italian Research Center on High Performance Computing, Big Data and Quantum Computing, funded by European Union – NextGenerationEU. S.S. acknowledges funding from ASI, Agenzia Spaziale Italiana (Grant No. DC-UOT-2018-024 – MUSICA – Multiband Ultrawide SpectroImager for Cryosphere Analysis).

APPENDIX A: EXPERIMENTAL DETAILS

The optical properties of QDs from samples with $x = 0.15$ Al content in the barrier and a miscut angle α of either 0° or 2° were investigated by means of polarization- and time-resolved photoluminescence (PL) spectroscopy. The sample was kept in a low-vibration closed-cycle He cryostat at a temperature of 5 K and excited via a 0.42 NA objective. The PL signal, collected through the same objective, was sent to a double-grating spectrometer with 1200 gr/mm gratings, resulting in a resolution of approximately 40 μeV near 1.6 eV. Spatial filtering passing through a single-mode fiber was occasionally employed.

For the fine structure splitting measurements, QDs were individually excited above barrier by a 532-nm continuous wave laser. The signal was acquired using a deep-depletion, back-illuminated LN2-cooled CCD. Several spectra were recorded by including a rotating half-wave plate and a linear polarizer in the collection path. This method allows to estimate the fine structure splitting [40] with an accuracy down to 1 μeV.

To estimate the radiative lifetime, the QDs were excited in pulsed mode using a Ti:sapphire laser, whose spectral width and pulse duration were adjusted to 200 μeV and 10 ps, respectively, in a $4f$ pulse shaper. The approach of resonant two-photon excitation [41] was chosen to avoid introducing time jittering due to the process of carrier relaxation from the barrier, while also conveniently suppressing laser background with notch filters. After selecting the emission line relative to the exciton to ground-state transition through the spectrometer, the PL signal is acquired by a single-photon counting module with a time resolution slightly above 50 ps. The radiative lifetime is estimated from a fit of the time-resolved PL curve with a convolution of the instrument response function (obtained recording the attenuated laser pulse) and an exponential decay. We assume a negligible impact of nonradiative recombination channels and scattering onto dark exciton states, consistently with previous studies [18].

APPENDIX B: COMPUTATIONAL METHODS

For each calculation, the GaAs QD is placed at the center of a simulation box containing $124a_0 \times 124a_0 \times 124a_0$ eight-atom zinc-blende unit cells (corresponding to nearly $1.5\ \times 10^7$ atoms) filled beforehand with the barrier material Al$_x$Ga$_{1-x}$As. a_0 refers to the lattice constant of the Al$_x$Ga$_{1-x}$As matrix. This procedure accurately captures the exact atomistic symmetry of the QD system, without any extra assumption. Note that we will refer here to the C_{3v} symmetry as the nominal symmetry, i.e., the QD symmetry of the system without taking into account the perturbations introduced by the surrounding Al$_x$Ga$_{1-x}$As matrix. Once the geometry of the system has been set up, the minimization of the strain energy is carried out via a generalized valence force field (GVFF) approach [42–44] which allows the ideal atomic positions to be relaxed. Then, the single-particle electron and hole states (ψ_j) and energies (E_j) are obtained by solving two times Schrödinger-Pauli's equation within the empirical pseudopotential framework:

$$\left[-\frac{\hbar^2}{2m_0}\nabla^2 + \sum_\alpha (v_\alpha(\boldsymbol{r}-\boldsymbol{r}_\alpha) + V_\alpha^{\mathrm{SO}}(\boldsymbol{r}-\boldsymbol{r}_\alpha))\right]\psi_j(\boldsymbol{r},\sigma) = E_j\psi_j(\boldsymbol{r},\sigma), \tag{B1}$$

where j denotes either the holes (h) or the electrons (e) depending on whether the calculation is performed for valence or conduction states. The first term is the kinetic energy (where m_0 represents the bare electronic mass and $\hbar$ denotes the reduced Planck constant) while $v_\alpha(\boldsymbol{r}-\boldsymbol{r}_\alpha)$ is the screened atomic pseudopotential for each atom of type α located at position $\boldsymbol{r}_\alpha$, i.e., a local potential fitted to experimentally known bulk quantities (such as energy band gaps, effective masses, and deformation potentials). Moreover, the spin of the wave function is described by the index $\sigma \in \{\uparrow, \downarrow\}$. Finally, the spin-orbit interaction is included as the only nonlocal part under the formal form [43,45–49]

$$V_\alpha^{\mathrm{SO}}(\boldsymbol{r}-\boldsymbol{r}_\alpha) = \sum_l |l\rangle V_{l,\alpha}^{\mathrm{SO}}(\boldsymbol{r}-\boldsymbol{r}_\alpha)\hat{\boldsymbol{L}}\cdot\hat{\boldsymbol{S}}\langle l|, \tag{B2}$$

in which $|l\rangle$ is the projection operator of orbital angular momentum l and only $l = 1$ is used in practice. Besides, $\hat{\boldsymbol{L}} \equiv (\hat{L}_x, \hat{L}_y, \hat{L}_z)$ is the orbital angular momentum vector operator, $\hat{\boldsymbol{S}} \equiv (\hat{S}_x, \hat{S}_y, \hat{S}_z)$ is the spin-vector operator, and $V_{l,\alpha}^{\mathrm{SO}}(r)$ is a potential describing the spin-orbit interaction (that we set to a Gaussian). The strained linear combination of bulk bands (SLCBB) method [50], which constitutes an efficient approach to handle multimillion-atom systems, is particularly suited to tackle the problem at hand and is employed here with a $10 \times 10 \times 10$ k-points grid centered around the Γ point. The resulting wave functions are subsequently plugged into a screened configuration interaction (CI) scheme [51,52] which can simulate Slater determinants from single-particle wave functions. Including Kramers spin, $N_v = 18$ valence states and $N_c = 18$ conduction states form the CI basis onto which the construction of the correlated (multi)exciton wave functions $|\Psi(X)\rangle$ relies. In this study, the exciton states $|\Psi(X^0)\rangle$ are of particular interest and the corresponding many-body wave functions are formally written

$$|\Psi(X^0)\rangle = \sum_{h_i}^{N_v}\sum_{e_j}^{N_c} A(h_i, e_j)|\Phi_{h_i,e_j}\rangle, \tag{B3}$$

where

$$|\Phi_{h_i,e_j}\rangle = \hat{d}^\dagger_{h_i}\hat{c}^\dagger_{e_j}|\Phi_0\rangle, \tag{B4}$$

and $\hat{d}^\dagger_{h_i}$ ($\hat{c}^\dagger_{e_j}$) is an operator that creates a hole (an electron) in the state ϕ_{h_i} (ϕ_{e_j}), while the $A(h_i, e_j)$ terms are coefficients accounting for the weight of each basis determinant $|\Phi_{h_i,e_j}\rangle$. In other words, Eq. (B4) describes the promotion of an electron from the valence state ϕ_{h_i} with energy E_{h_i} to a conduction state ϕ_{e_j} with energy E_{e_j}. Here, the ϕ states are spinors related to the ψ states by the relationship

$$\phi(\boldsymbol{r}) = \begin{pmatrix}\psi(\boldsymbol{r},\uparrow)\\ \psi(\boldsymbol{r},\downarrow)\end{pmatrix}. \tag{B5}$$

Thus, the sum in Eq. (B3) runs over all the 36 (conduction and valence) states that are used to produce singly excited Slater determinants from the ground-state Slater determinant $|\Phi_0\rangle$ (or equivalently the Fermi vacuum state in the electron-hole picture). The many-body Hamiltonian $\widehat{\mathcal{H}}$ is then diagonalized in the CI basis and its matrix elements can be extracted from the following formula [51,53]:

$$\begin{aligned}\mathcal{H}_{he,h'e'} &= \langle\Phi_{h,e}|\widehat{\mathcal{H}}|\Phi_{h',e'}\rangle,\\ &= (E_e - E_h)\delta_{hh'}\delta_{ee'} - J_{he,h'e'} + K_{he,h'e'}.\end{aligned} \tag{B6}$$

Here, $\delta_{jj'}$ symbolizes the Kronecker delta while the J and K terms represent the electron-hole direct and exchange Coulomb integrals, respectively, and their matrix elements can be calculated as [51]

$$J_{he,h'e'} = \frac{e^2}{4\pi\epsilon_0}\sum_{\sigma_1,\sigma_2}\iint d\boldsymbol{r}_1 d\boldsymbol{r}_2 \frac{\psi^*_{h'}(\boldsymbol{r}_1,\sigma_1)\psi^*_{e}(\boldsymbol{r}_2,\sigma_2)\psi_h(\boldsymbol{r}_1,\sigma_1)\psi_{e'}(\boldsymbol{r}_2,\sigma_2)}{\epsilon(\boldsymbol{r}_1,\boldsymbol{r}_2)|\boldsymbol{r}_1-\boldsymbol{r}_2|}, \tag{B7}$$

$$K_{he,h'e'} = \frac{e^2}{4\pi\epsilon_0}\sum_{\sigma_1,\sigma_2}\iint d\boldsymbol{r}_1 d\boldsymbol{r}_2 \frac{\psi^*_{h'}(\boldsymbol{r}_1,\sigma_1)\psi^*_{e}(\boldsymbol{r}_2,\sigma_2)\psi_{e'}(\boldsymbol{r}_1,\sigma_1)\psi_{h}(\boldsymbol{r}_2,\sigma_2)}{\epsilon(\boldsymbol{r}_1,\boldsymbol{r}_2)|\boldsymbol{r}_1-\boldsymbol{r}_2|}, \tag{B8}$$

where e is the elementary charge of the electron and ϵ_0 is the permittivity of free space while $\epsilon(\boldsymbol{r}_1,\boldsymbol{r}_2)$ is a screening function based on the Thomas-Fermi model for semiconductors first introduced by Resta [54]. Once all these steps have been performed, accessing the theoretical PL emission and the fine structure of the exciton [52] is straightforward. As for the radiative lifetime $\tau_{if}(X^0_\nu)$, the calculation is carried out according to the formula [55]

$$\frac{1}{\tau_{if}\left(X^0_\nu\right)} = \frac{e^2 n_{\mathrm{QD}}}{3\pi\epsilon_0 m_0^2 c_0^3 \hbar^2} E_{if}\left(X^0_\nu\right)\sum_{\boldsymbol{e}=\boldsymbol{e}_x,\boldsymbol{e}_y,\boldsymbol{e}_z}\left|M^{\boldsymbol{e}}_{if}\left(X^0_\nu\right)\right|^2, \tag{B9}$$

with

$$M^{\boldsymbol{e}}_{if}\left(X^0_\nu\right) = \left\langle\Psi\left(X^0_\nu\right)|\boldsymbol{e}\cdot\hat{\boldsymbol{p}}|\Phi_0\right\rangle. \tag{B10}$$

In Eqs. (B9) and (B10), n_{QD} is the refractive index of GaAs, $E_{if}(X^0_\nu)$ is the energy of the transition, c_0 is the speed of light in vacuum, $\boldsymbol{e}$ is a polarization unit vector, while $\hat{\boldsymbol{p}} = -i\hbar\nabla$ is the momentum operator which commonly appears in the electric dipole transition matrix elements. The subscript ν indicates a specific state of the exciton manifold (consisting here of two dark states and two bright states). Note that Eq. (B9) strictly describes the characteristic radiative recombination rate of the transition $|\Psi(X^0_\nu)\rangle \rightarrow |\Phi_0\rangle$. In order to take into account the populations of each state in the calculation of the radiative lifetime, a model including rate equations must be used [56], which is out of the scope of this study. Our simpler model is nonetheless sufficient to provide insightful comparison with our experiments, as detailed in Appendix A.

Finally, we will characterize the optical anisotropy by the degree of linear polarization (DLP) which is defined in the $[1\bar{1}0]$-$[11\bar{2}]$ plane as

$$\mathrm{DLP} = \frac{I_{\max} - I_{\min}}{I_{\max} + I_{\min}}, \tag{B11}$$

where $I_{\max}$ ($I_{\min}$) represents the maximum (minimum) intensity of the polarization ellipse.

APPENDIX C: SINGLE-PARTICLE WAVE FUNCTIONS: FROM THE 2D QUANTUM HARMONIC OSCILLATOR TO THE ATOMISTIC C_{3v} EPM RESULTS

In this Appendix, we provide more details on the EPM single-particle wave functions. The 18 first single-particle conduction and valence states used to form our CI basis for the quantum dot with $x = 1.00$ are shown, respectively, in Figs. 8 and 9. The corresponding states for $x = 0.15$ are plotted in Figs. 10 and 11. For a quantum dot with hexagonal shape, large in-plane diameter (≈70 nm) and small height (≈4 nm), a model based on a two-dimensional parabolic potential confinement constitutes a reasonable starting point to understand the single-particle physics. Hence, we propose to analyze our results in light of a widely known simplified model whose main features are reminded thereafter.

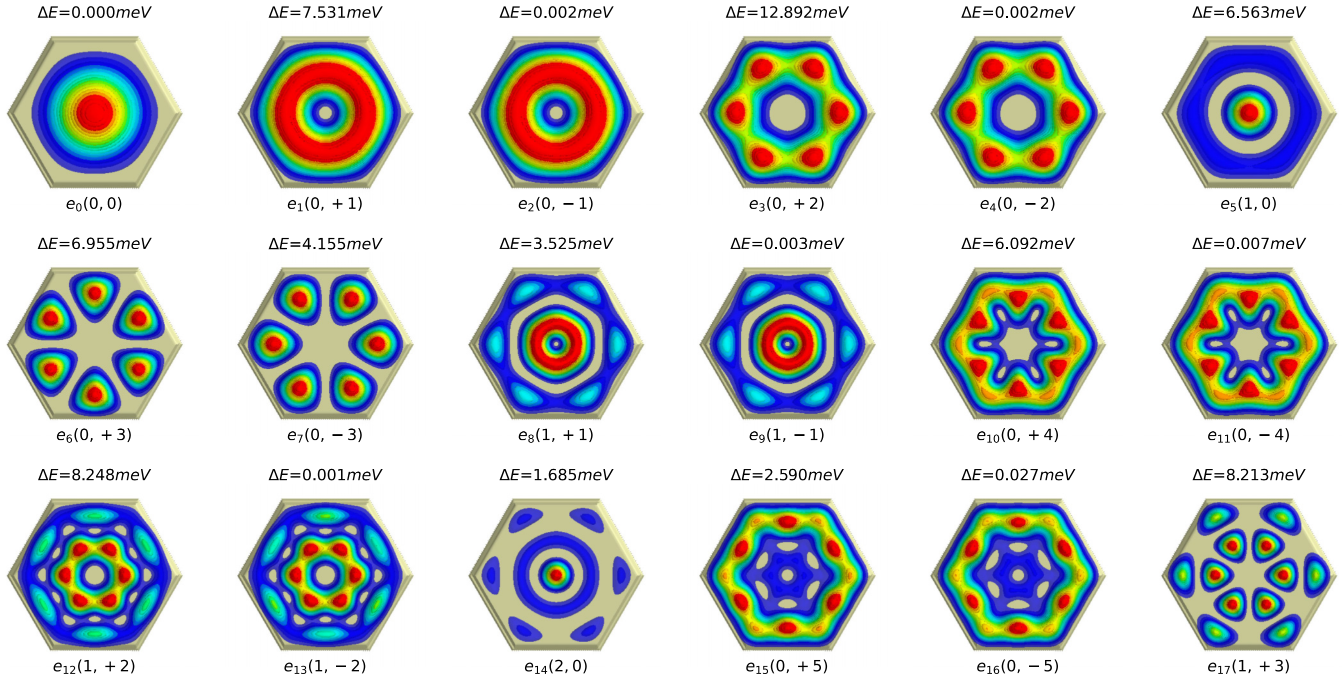

FIG. 8. Cross sections in the (111) plane of the 18 first single-particle electron-squared wave functions for a GaAs/AlAs QD. At the top of each plot is given the energy splitting with respect to the previous state. The bottom labels indicate the radial and azimuthal quantum numbers associated with the state in the Fock-Darwin notation (n_r, l) (see text).

The solution of the Schrödinger's equation for a two-dimensional isotropic quantum harmonic oscillator (2D-QHO) is given by the Fock-Darwin states which can be expressed in polar coordinates (r, ϕ) as [22]

$$\psi_{n_r,l}(r,\phi) = \frac{\beta}{\sqrt{2\pi}}\sqrt{\frac{n_r!}{(n_r+|l|)!}}\, e^{-\frac{\beta^2 r^2}{4}}\, e^{il\phi}\left(\frac{\beta r}{\sqrt{2}}\right)^{|l|}$$

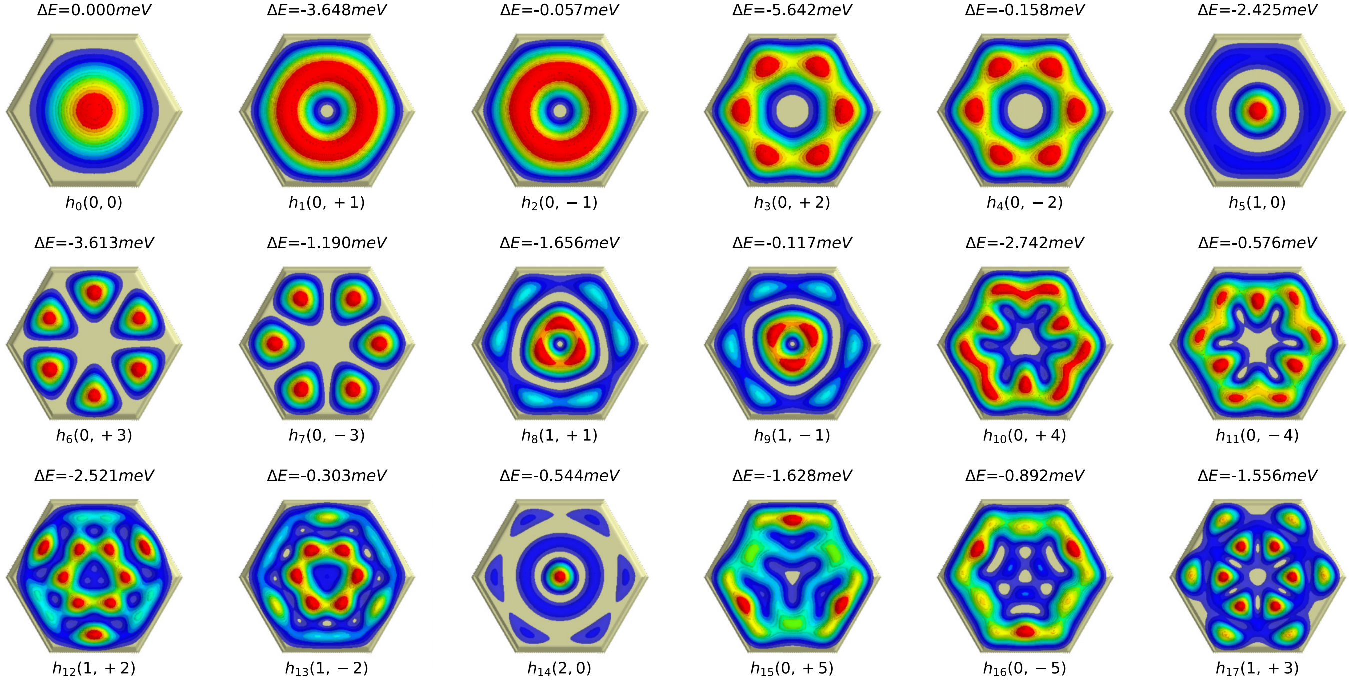

FIG. 9. Cross sections in the (111) plane of the 18 first single-particle hole-squared wave functions for a GaAs/AlAs QD. At the top of each plot is given the energy splitting with respect to the previous state. The bottom labels indicate the radial and azimuthal quantum numbers associated with the state in the Fock-Darwin notation (n_r, l) (see text).

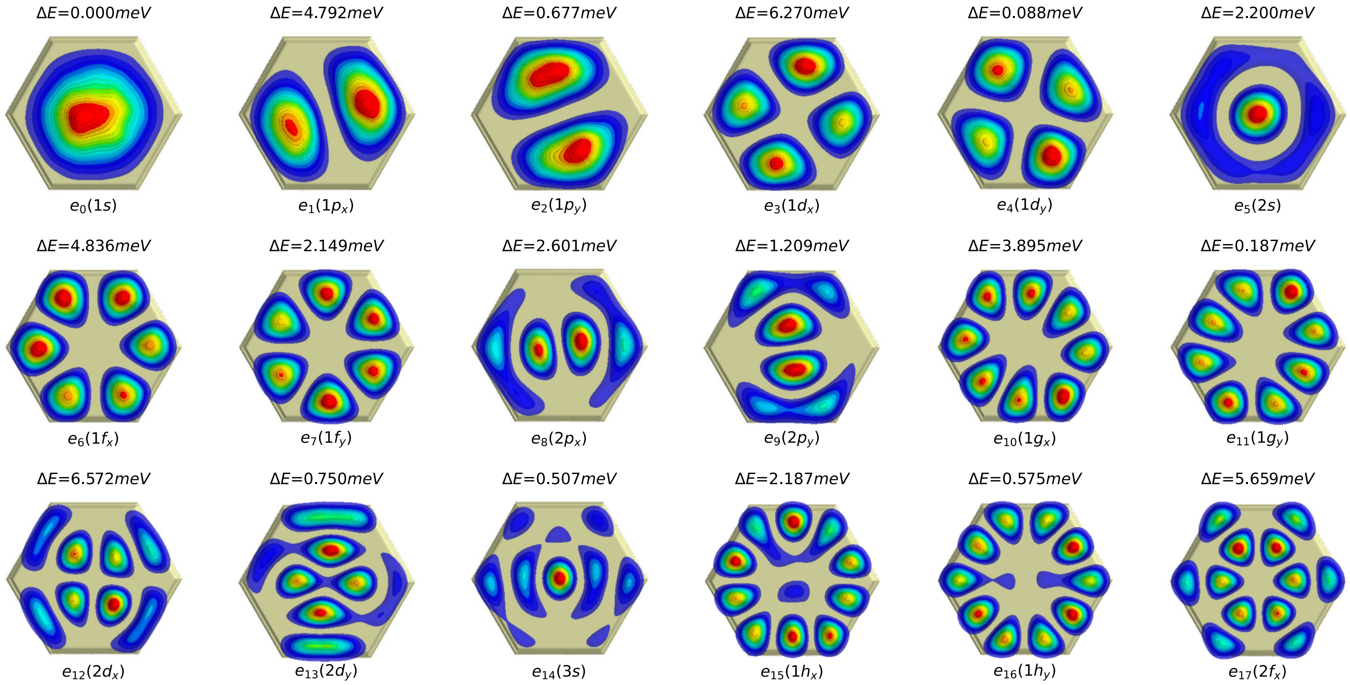

FIG. 10. Cross sections in the (111) plane of the 18 first single-particle electron-squared wave functions for a GaAs/$\mathrm{Al}_{0.15}\mathrm{Ga}_{0.85}$As QD. At the top of each plot is given the energy splitting with respect to the previous state. The bottom labels are inspired from the atomic physics notation: s, p, d, f, g, h.

$$\times\ L_{n_r}^{|l|}\left(\frac{\beta^2 r^2}{2}\right), \qquad \text{(C1)}$$

where n_r and l are, respectively, the radial and azimuthal quantum numbers. Visually, n_r can be interpreted as the number of nodes in the wave function in the radial direction. l determines the size of the dip in the center and the radial extent of the wave function (see, e.g., Fig. 6 of Ref. [22]). These two quantum numbers will be used to label the states for the GaAs/AlAs(111) QD in order to highlight the similarities

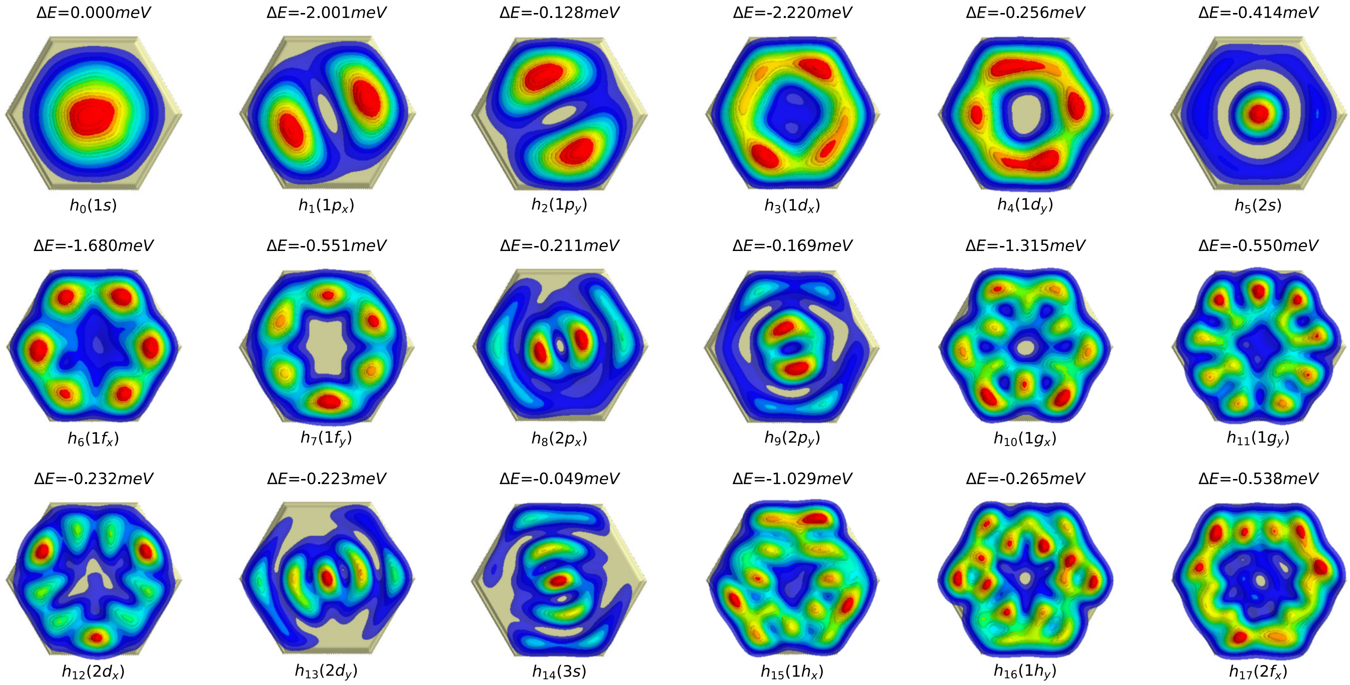

FIG. 11. Cross sections in the (111) plane of the 18 first single-particle hole-squared wave functions for a GaAs/$\mathrm{Al}_{0.15}\mathrm{Ga}_{0.85}$As QD. At the top of each plot is given the energy splitting with respect to the previous state. The bottom labels are inspired from the atomic physics notation: s, p, d, f, g, h.

TABLE II. Fock-Darwin states and their energies.

(n_r, l)	$E_{2D}(n_r, l)$
(0,0)	1 $\hbar\omega$
(0, ±1)	2 $\hbar\omega$
(0, ±2); (1,0)	3 $\hbar\omega$
(0, ±3); (1, ±1)	4 $\hbar\omega$
(0, ±4); (1, ±2); (2,0)	5 $\hbar\omega$
(0, ±5); (1, ±3); (2, ±1)	6 $\hbar\omega$

between the 2D-QHO model and our results. $\beta = \sqrt{m\omega/\hbar}$ is a constant for a given material, m being its effective mass while ω is the oscillator frequency. The $L_{n_r}^{|l|}(\cdot)$ functions are generalized Laguerre polynomials. The corresponding energies are given by

$$E_{2D}(n_r, l) = (2n_r + |l| + 1)\hbar\omega. \tag{C2}$$

From Eq. (C2) it is evident that there exist degenerate levels in the 2D-QHO, which are listed in Table II together with their respective energies. It implies that (i) energy levels for which $2n_r + |l| =$ const are degenerate and (ii) nondegenerate energy levels are equally spaced (by steps of $\hbar\omega$).

It is manifest from Eq. (C1) that $|\psi_{n_r,l}(r,\phi)|^2 = |\psi_{n_r,-l}(r,\phi)|^2$. This equality means that for a given value of n_r, the two densities of probability for l and $-l$ will be identical. We recall here that this model is valid for a quantum system with cylindrical symmetry ($C_{\infty v}$) and neglects atomistic effects by making use of an effective mass framework. Thus, it would be unexpected that such a simple model could provide insights to understand the physics of realistic nanostructures. Nonetheless, both the conduction and valence states for $x = 1.00$ states look remarkably similar to the description given by $|\psi_{n_r,l}(r,\phi)|^2$ (but without the perfect cylindrical symmetry $C_{\infty v}$). They are also energetically ordered in the same way although the energy splittings between the states are not equidistant and certain degeneracies are lifted, which points out a first limitation of the 2D-QHO approach.

Now, let us emphasize these differences by looking more closely at the atomistic results in order to see how the symmetry reduction $C_{\infty v} \rightarrow C_{6v} \rightarrow C_{3v} \rightarrow C_s$ affects the wave functions. The QDs investigated in this work differ from this idealized picture in two aspects: the hexagonal geometry of the base lowers the symmetry to C_{6v} while the crystal atomistic structure of the underlying zinc-blende lattice in [111] further reduces it to the C_{3v} point group [57]. Note that for a system quantized along [111] in a cubic simulation box, it is estimated that the SLCBB code can resolve energy splittings down to $\Delta E \approx 30$–40 μeV, such that two states with an energy splitting below this threshold will be considered degenerate.

Consider the $x = 1.00$ case. All the 18 conduction states plotted in Fig. 8 exhibit a very clear C_{6v} symmetry. In other words, their symmetry is determined only by the hexagonal geometry of the quantum dot base. This observation comes as a surprise as it indicates that the electron states are only sensitive to the QD shape and do not feel the actual crystal symmetry, in striking contrast with lens-shaped QD grown along [001] [57]. Moreover, a large amount of the symmetries predicted for the $C_{\infty v}$ systems by the 2D-QHO model are retained. Indeed, for a given value of n_r, most of the states of the form $(n_r, \pm l)$ are degenerate (with the notable exception of $|l| = 3$). Once again, we point out that despite these similarities with the 2D-QHO model, the advanced calculations show also manifest differences since the states with $n_r \neq 0$ and $l = 0$ are never degenerate and the states with $\Delta l = 1$ are not equidistant in energy.

On the other hand, when the valence states are considered (see Fig. 9), all the degeneracies are lifted although the first eight states are almost identical to the conduction states and possess the C_{6v} symmetry. On the contrary, the higher-energy states with opposite azimuthal quantum number are now distinct and their symmetry is lowered to C_{3v}, showing that the hole states are actually sensitive to the crystal lattice symmetry. For example, by summing the valence states $(1, +1)$ and $(1, -1)$, one can see that the the resulting state will look like the conduction states $(1, \pm1)$. The same observation can be made for $(0, \pm4)$, $(1, \pm2)$, and $(0, \pm5)$, i.e., all the valence states which have the C_{3v} symmetry. The origin of this behavior is yet to be elucidated.

For the GaAs/Al$_x$Ga$_{1-x}$As(111) QDs with $x = 0.15$, the rotational symmetry is broken and the Fock-Darwin notation (n_r, l) is no longer meaningful. Instead, a notation inspired from atomic physics (s, p, d, f, g, h) is adopted in Figs. 10 and 11. By comparing Fig. 10 with Fig. 8, it is clear that the ground state e_0 is a 1s state with only a distortion compared to the (0,0) state. Besides, the $(0, \pm1)$ states are evidently split into two *p-like* states labeled 1p_x and 1p_y whose orientation depends on the arrangement of the atoms in the disordered barrier material surrounding the quantum dots. The same observation is valid for the $(0, \pm2)$ states which become *d-like* states. Higher energetic states also follow the same pattern. Note that the $(1, \pm1)$ can be thought as a linear combination of 1p states, as for an ensemble of QDs with $x = 0.15$ averaged over a large number of random distributions there would be no privileged orientation.

In conclusion, we have shown in this Appendix that (i) the 2D-QHO toy model constitutes a reasonable approximation which can provide preliminary interesting insights to grasp the physics of realistic C_{3v} systems, (ii) the conduction states of hexagonal-based GaAs/AlAs(111) QD have the same symmetry of the QD shape C_{6v}, and (iii) the hole is more sensitive to the atomistic crystal lattice symmetry C_{3v}, which is the expected result from group theory and previous works [57].

APPENDIX D: RELATIONSHIP BETWEEN THE CONTRAST IN LIFETIME AND THE DEGREE OF LINEAR POLARIZATION

In this Appendix, we present a simple relationship connecting the contrast in lifetime to the degree of linear polarization in self-assembled quantum dots using only a single assumption, based on the argument developed in Ref. [31] that two exciton states belonging to different irreducible representations must have different characteristic lifetimes.

The prototypical nanostructure that is considered in the following derivation is a quantum system with a fourfold nondegenerate exciton ground state. It is assumed that the two dark states X_1 and X_2, which are lower in energy, can safely be neglected hereafter owing to their very small transition dipole moments in the absence of dark-bright exciton coupling. We will therefore focus on the two bright states X_3 and X_4 which are the optically active ones. Their respective energies are such that $E_{X_1} \leqslant E_{X_2} < E_{X_3} < E_{X_4}$ as hinted by the notation. The main assumption that will be used later on is that the two transitions $|X_3\rangle \rightarrow |\Phi_0\rangle$ and $|X_4\rangle \rightarrow |\Phi_0\rangle$, where Φ_0 is the ground state, have orthogonal polarizations. Such a condition is usually fulfilled when the exciton ground state possesses a pure heavy-hole character, but it is not restricted to this case. We show below that it is possible for these systems to derive an analytical formula connecting the degree of linear polarization to the contrast in lifetime.

Starting with Eq. (B9) and setting $\kappa = \frac{e^2 n_{\mathrm{QD}}}{3\pi\epsilon_0 m_0^2 c_0^3 \hbar^2}$, one can write the recombination decay rates for the two bright exciton states as

$$\frac{1}{\tau_{X_{3,4}}} = \kappa E_{X_{3,4}} \sum_{e=\boldsymbol{e}_x,\boldsymbol{e}_y,\boldsymbol{e}_z} |M^e(X_{3,4})|^2. \tag{D1}$$

The contrast in lifetime can be expressed in general as

$$C_\tau = \frac{\tau_{X_3} - \tau_{X_4}}{\tau_{X_3} + \tau_{X_4}}. \tag{D2}$$

For a quantum dot with C_{3v} symmetry, the two bright exciton states X_3 and X_4 belong to the same irreducible representation of the point group so that $\tau_{X_3} = \tau_{X_4}$ and $C_\tau = 0$. When this symmetry is broken, a lifetime asymmetry can exist and $C_\tau \neq 0$ (for example, in the main body of the text, it is lowered to C_s by introducing a miscut angle $\alpha \neq 0^\circ$). Defining $I_{X_i} \equiv \sum_{e=\boldsymbol{e}_x,\boldsymbol{e}_y,\boldsymbol{e}_z} |M^e(X_i)|^2$ and using Eq. (D1), the expression of C_τ in Eq. (D2) can be rewritten as

$$\begin{aligned} C_\tau &= \frac{\frac{1}{\kappa E_{X_3} I_{X_3}} - \frac{1}{\kappa E_{X_4} I_{X_4}}}{\frac{1}{\kappa E_{X_3} I_{X_3}} + \frac{1}{\kappa E_{X_4} I_{X_4}}} \\ &= \frac{E_{X_4} I_{X_4} - E_{X_3} I_{X_3}}{E_{X_4} I_{X_4} + E_{X_3} I_{X_3}} \\ &= \frac{I_{X_4} - I_{X_3}(E_{X_4}/E_{X_3})}{I_{X_4} + I_{X_3}(E_{X_4}/E_{X_3})}. \end{aligned} \tag{D3}$$

Since $E_{X_4}/E_{X_3} = 1 + \mathrm{FSS}/E_{X_3}$ and $\mathrm{FSS}/E_{X_3} \approx 10^{-5} \ll 1$, the equation for the contrast in lifetime is finally given by

$$C_\tau = \frac{I_{X_4} - I_{X_3}}{I_{X_4} + I_{X_3}}. \tag{D4}$$

Besides, in the $[1\bar{1}0]$-$[11\bar{2}]$ plane, the optical anisotropy can be characterized by the degree of linear polarization as follows:

$$\mathrm{DLP} = \frac{I_{[1\bar{1}0]} - I_{[11\bar{2}]}}{I_{[1\bar{1}0]} + I_{[11\bar{2}]}}, \tag{D5}$$

where the intensities are simply related to the transition dipole matrix elements by

$$\begin{aligned} I_{[1\bar{1}0]} &= \sum_{i=3,4} |M^{[1\bar{1}0]}(X_i)|^2, \\ I_{[11\bar{2}]} &= \sum_{i=3,4} |M^{[11\bar{2}]}(X_i)|^2. \end{aligned} \tag{D6}$$

Note also that the two definitions of the DLP given by Eqs. (B11) and (D5) become equivalent if and only if the polarizations of the two bright transitions are orthogonal to each other. Indeed, under this condition, $I_{\max}$ will coincide either with $I_{[1\bar{1}0]}$ or $I_{[11\bar{2}]}$ (and conversely for $I_{\min}$).

If the intensities I_{X_3} and I_{X_4} can be written as functions of $I_{[1\bar{1}0]}$ and $I_{[11\bar{2}]}$, then the DLP and C_τ can be connected to each other. In general, finding a direct correlation between these two quantities is not possible. However, when X_3 is entirely polarized along $\boldsymbol{e}_x = [1\bar{1}0]$ whereas X_4 is completely polarized along $\boldsymbol{e}_y = [11\bar{2}]$ as this is the case in this study and in Ref. [29] (where polar diagrams are provided), the following approximations can be introduced:

$$\begin{aligned} |M^{[11\bar{2}]}(X_3)| &= |M^{[111]}(X_3)| = 0, \\ |M^{[1\bar{1}0]}(X_4)| &= |M^{[111]}(X_4)| = 0. \end{aligned} \tag{D7}$$

Equation (D7) is the key assumption to relate the contrast in lifetime C_τ to the DLP as it straightforwardly leads to

$$\begin{cases} I_{X_3} = |M^{[1\bar{1}0]}(X_3)|^2 = I_{[1\bar{1}0]}, \\ I_{X_4} = |M^{[11\bar{2}]}(X_4)|^2 = I_{[11\bar{2}]}. \end{cases} \tag{D8}$$

Under this hypothesis, τ_{X_3} and τ_{X_4} can be relabeled as $\tau_{[1\bar{1}0]}$ and $\tau_{[11\bar{2}]}$, respectively, so that a more convenient expression for the contrast in lifetime can be formulated:

$$C_\tau = \frac{\tau_{[1\bar{1}0]} - \tau_{[11\bar{2}]}}{\tau_{[1\bar{1}0]} + \tau_{[11\bar{2}]}}. \tag{D9}$$

And, finally, using Eqs. (D4) and (D8),

$$\begin{aligned} C_\tau &= \frac{I_{[11\bar{2}]} - I_{[1\bar{1}0]}}{I_{[1\bar{1}0]} + I_{[11\bar{2}]}} \\ &= -\mathrm{DLP}. \end{aligned} \tag{D10}$$

The presence of a minus sign in Eq. (D10) is related to the ordering of the polarizations for the X_3 and X_4 states. If, for a given quantum dot, $I_{X_3} = I_{[11\bar{2}]}$ and $I_{X_4} = I_{[1\bar{1}0]}$, then one would get $C_\tau = \mathrm{DLP}$. Nonetheless, when taking the absolute value, the relationship between the contrast in lifetime and the DLP obtained here is the same as in Eq. (12) in Ref. [31]. The latter formula was derived using an effective model to describe the optical properties of InGaAs QDs grown along [001] with C_{2v} nominal symmetry.

Our numerical results and the above analytical derivation demonstrate that this equality can be generalized to any quantum dot whose optically active excitonic structure consists of two bright states with orthogonal polarizations. This conclusion does not rely on any specific model and is valid as long as Eq. (D1) constitutes a reasonable definition for the lifetime.

Finally, note that in Ref. [31] perturbations lowering the QD symmetry from C_{2v} to C_1 are considered via an angle θ. The latter accounts for deviations of the exciton polarization angle from the main symmetry axes ($[1\bar{1}0]$ and [110]) and allows to distinguish between extrinsic and intrinsic lifetimes. This distinction is not addressed in our proof.

[1] D. Loss and D. P. DiVincenzo, Quantum computation with quantum dots, Phys. Rev. A **57**, 120 (1998).

[2] O. Benson, C. Santori, M. Pelton, and Y. Yamamoto, Regulated and Entangled Photons from a Single Quantum Dot, Phys. Rev. Lett. **84**, 2513 (2000).

[3] A. Orieux, M. A. Versteegh, K. D. Jöns, and S. Ducci, Semiconductor devices for entangled photon pair generation: a review, Rep. Prog. Phys. **80**, 076001 (2017).

[4] Y. Li, F. Ding, and O. G. Schmidt, Entangled-photons generation with quantum dots, Chin. Phys. B **27**, 020307 (2018).

[5] D. Huber, M. Reindl, J. Aberl, A. Rastelli, and R. Trotta, Semiconductor quantum dots as an ideal source of polarization-entangled photon pairs on-demand: a review, J. Opt. **20**, 073002 (2018).

[6] C. Schimpf, M. Reindl, F. Basso Basset, K. D. Jöns, R. Trotta, and A. Rastelli, Quantum dots as potential sources of strongly entangled photons: Perspectives and challenges for applications in quantum networks, Appl. Phys. Lett. **118**, 100502 (2021).

[7] J. Neuwirth, F. Basso Basset, M. B. Rota, E. Roccia, C. Schimpf, K. D. Jöns, A. Rastelli, and R. Trotta, Quantum dot technology for quantum repeaters: from entangled photon generation toward the integration with quantum memories, Mater. Quantum. Technol. **1**, 043001 (2021).

[8] D. A. Vajner, L. Rickert, T. Gao, K. Kaymazlar, and T. Heindel, Quantum communication using semiconductor quantum dots, Adv. Quantum Technol. **5**, 2100116 (2022).

[9] R. Singh and G. Bester, Nanowire Quantum Dots as an Ideal Source of Entangled Photon Pairs, Phys. Rev. Lett. **103**, 063601 (2009).

[10] M. Abbarchi, T. Kuroda, T. Mano, and K. Sakoda, Fine structure splitting reduction in droplet epitaxy GaAs quantum dots grown on (111)A surface, J. Phys. Chem. Sol. **245**, 012049 (2010).

[11] T. Mano, M. Abbarchi, T. Kuroda, B. McSkimming, A. Ohtake, K. Mitsuishi, and K. Sakoda, Self-assembly of symmetric GaAs quantum dots on (111)A substrates: Suppression of fine-structure splitting, Appl. Phys. Express **3**, 065203 (2010).

[12] X. Liu, N. Ha, H. Nakajima, T. Mano, T. Kuroda, B. Urbaszek, H. Kumano, I. Suemune, Y. Sakuma, and K. Sakoda, Vanishing fine-structure splittings in telecommunication-wavelength quantum dots grown on (111)A surfaces by droplet epitaxy, Phys. Rev. B **90**, 081301(R) (2014).

[13] T. Chikyow and N. Koguchi, MBE growth method for pyramid-shaped GaAs micro crystals on ZnSe (001) surface using Ga droplets, Jpn. J. Appl. Phys. **29**, L2093 (1990).

[14] N. Koguchi, K. Ishige, and S. Takahashi, New selective molecular-beam epitaxial growth method for direct formation of GaAs quantum dots, J. Vac. Sci. Technol. B **11**, 787 (1993).

[15] M. Jo, T. Mano, M. Abbarchi, T. Kuroda, Y. Sakuma, and K. Sakoda, Self-limiting growth of hexagonal and triangular quantum dots on (111) A, Cryst. Growth Des. **12**, 1411 (2012).

[16] A. Tuktamyshev, A. Fedorov, S. Bietti, S. Tsukamoto, and S. Sanguinetti, Temperature activated dimensionality crossover in the nucleation of quantum dots by droplet epitaxy on GaAs (111)A vicinal substrates, Sci. Rep. **9**, 14520 (2019).

[17] A. Trapp and D. Reuter, Formation of self-assembled GaAs quantum dots via droplet epitaxy on misoriented GaAs(111)B substrates, J. Vac. Sci. Technol. B **36**, 02D106 (2018).

[18] F. Basso Basset, S. Bietti, M. Reindl, L. Esposito, A. Fedorov, D. Huber, A. Rastelli, E. Bonera, R. Trotta, and S. Sanguinetti, High-yield fabrication of entangled photon emitters for hybrid quantum networking using high-temperature droplet epitaxy, Nano Lett. **18**, 505 (2018).

[19] S. Bietti, F. Basso Basset, A. Tuktamyshev, E. Bonera, A. Fedorov, and S. Sanguinetti, High–temperature droplet epitaxy of symmetric GaAs/AlGaAs quantum dots, Sci. Rep. **10**, 6532 (2020).

[20] V. Fock, Bemerkung zur Quantelung des harmonischen Oszillators im Magnetfeld, Z. Phys. **47**, 446 (1928).

[21] C. G. Darwin, The diamagnetism of the free electron, Math. Proc. Cambridge Philos. Soc. **27**, 8690 (1931).

[22] L. P. Kouwenhoven, D. G. Austing, and S. Tarucha, Few-electron quantum dots, Rep. Prog. Phys. **64**, 701 (2001).

[23] P. Ramachandran and G. Varoquaux, Mayavi: 3D visualization of scientific data, Comput. Sci. Eng. **13**, 40 (2011).

[24] N. Akopian, U. Perinetti, L. Wang, A. Rastelli, O. Schmidt, and V. Zwiller, Tuning single GaAs quantum dots in resonance with a Rubidium vapor, Appl. Phys. Lett. **97**, 082103 (2010).

[25] N. Akopian, L. Wang, A. Rastelli, O. G. Schmidt, and V. Zwiller, Hybrid semiconductor-atomic interface: slowing down single photons from a quantum dot, Nat. Photon. **5**, 230 (2011).

[26] R. Trotta, J. Martín-Sánchez, J. S. Wildmann, G. Piredda, M. Reindl, C. Schimpf, E. Zallo, S. Stroj, J. Edlinger, and A. Rastelli, Wavelength-tunable sources of entangled photons interfaced with atomic vapours, Nat. Commun. **7**, 10375 (2016).

[27] H. Huang, R. Trotta, Y. Huo, T. Lettner, J. S. Wildmann, J. Martín-Sánchez, D. Huber, M. Reindl, J. Zhang, E. Zallo, *et al.*, Electrically-pumped wavelength-tunable GaAs quantum dots interfaced with Rubidium atoms, ACS Photon. **4**, 868 (2017).

[28] R. Keil, M. Zopf, Y. Chen, B. Höfer, J. Zhang, F. Ding, and O. G. Schmidt, Solid-state ensemble of highly entangled photon sources at Rubidium atomic transitions, Nat. Commun. **8**, 15501 (2017).

[29] A. Barbiero, A. Tuktamyshev, G. Pirard, J. Huwer, T. Müller, R. M. Stevenson, S. Bietti, S. Vichi, A. Fedorov, G. Bester, S. Sanguinetti, and A. Shields, Exciton Fine Structure in InAs Quantum Dots with Cavity-Enhanced Emission at Telecommunication Wavelength and Grown on a GaAs(111)A Vicinal Substrate, Phys. Rev. Appl. **18**, 034081 (2022).

[30] M. Abbarchi, T. Mano, T. Kuroda, A. Ohtake, and K. Sakoda, Polarization anisotropies in strain-free, asymmetric, and symmetric quantum dots grown by droplet epitaxy, Nanomaterials **11**, 443 (2021).

[31] W. Xiong, X. Xu, J.-W. Luo, M. Gong, S.-S. Li, and G.-C. Guo, Fundamental Intrinsic Lifetimes in Semiconductor Self-Assembled Quantum Dots, Phys. Rev. Appl. **10**, 044009 (2018).

[32] A. J. Hudson, R. M. Stevenson, A. J. Bennett, R. J. Young, C. A. Nicoll, P. Atkinson, K. Cooper, D. A. Ritchie, and A. J. Shields, Coherence of an Entangled Exciton-Photon State, Phys. Rev. Lett. **99**, 266802 (2007).

[33] R. M. Stevenson, A. J. Hudson, A. J. Bennett, R. J. Young, C. A. Nicoll, D. A. Ritchie, and A. J. Shields, Evolution of Entanglement Between Distinguishable Light States, Phys. Rev. Lett. **101**, 170501 (2008).

[34] H. Chen, Z. Zhuo, J. Huang, X. Dou, X. He, K. Ding, H. Ni, Z. Niu, D. Jiang, and B. Sun, Correlation between exciton polarized lifetime and fine structure splitting in InAs/GaAs quantum dots, Appl. Phys. Lett. **116**, 082101 (2020).

[35] 1 ML along [111] is equal to $a_0/\sqrt{3}$ and l_{step} is obtained from $\tan(\alpha) = 1\ \text{ML}/l_{\text{step}}$. The QD length L along $[11\bar{2}]$ is equal to $\sqrt{3}d/2$, from which we calculate n_{steps} as L/l_{step}.

[36] D. Huber, B. U. Lehner, D. Csontosová, M. Reindl, S. Schuler, S. F. C. Da Silva, P. Klenovský, and A. Rastelli, Single-particle-picture breakdown in laterally weakly confining GaAs quantum dots, Phys. Rev. B **100**, 235425 (2019).

[37] P. A, Labud, A. Ludwig, A. D. Wieck, G. Bester, and D. Reuter, Direct Quantitative Electrical Measurement of Many-Body Interactions in Exciton Complexes in InAs Quantum Dots, Phys. Rev. Lett. **112**, 046803 (2014).

[38] N. Rivera and I. Kaminer, Light–matter interactions with photonic quasiparticles, Nat. Rev. Phys. **2**, 538 (2020).

[39] P. Tighineanu, R. Daveau, E. H. Lee, J. D. Song, S. Stobbe, and P. Lodahl, Decay dynamics and exciton localization in large GaAs quantum dots grown by droplet epitaxy, Phys. Rev. B **88**, 155320 (2013).

[40] M. Abbarchi, C. A. Mastrandrea, T. Kuroda, T. Mano, K. Sakoda, N. Koguchi, S. Sanguinetti, A. Vinattieri, and M. Gurioli, Exciton fine structure in strain-free GaAs/$Al_{0.3}Ga_{0.7}As$ quantum dots: Extrinsic effects, Phys. Rev. B **78**, 125321 (2008).

[41] H. Jayakumar, A. Predojević, T. Huber, T. Kauten, G. S. Solomon, and G. Weihs, Deterministic Photon Pairs and Coherent Optical Control of a Single Quantum Dot, Phys. Rev. Lett. **110**, 135505 (2013).

[42] P. N. Keating, Effect of invariance requirements on the elastic strain energy of crystals with application to the diamond structure, Phys. Rev. **145**, 637 (1966).

[43] A. J. Williamson, L.-W. Wang, and A. Zunger, Theoretical interpretation of the experimental electronic structure of lens-shaped self-assembled InAs/GaAs quantum dots, Phys. Rev. B **62**, 12963 (2000).

[44] J.-W. Luo, G. Bester, and A. Zunger, Atomistic Pseudopotential Theory of Droplet Epitaxial GaAs/AlGaAs Quantum Dots, in *Nanodroplets*, edited by Z. M. Wang (Springer, New York, 2013), pp. 329–361.

[45] L. Kleinman, Relativistic norm-conserving pseudopotential, Phys. Rev. B **21**, 2630 (1980).

[46] L. Kleinman and D. M. Bylander, Efficacious Form for Model Pseudopotentials, Phys. Rev. Lett. **48**, 1425 (1982).

[47] G. B. Bachelet and M. Schlüter, Relativistic norm-conserving pseudopotentials, Phys. Rev. B **25**, 2103 (1982).

[48] M. S. Hybertsen and S. G. Louie, Spin-orbit splitting in semiconductors and insulators from the ab initio pseudopotential, Phys. Rev. B **34**, 2920 (1986).

[49] G. Bester, Electronic excitations in nanostructures: an empirical pseudopotential based approach, J. Phys.: Condens. Matter **21**, 023202 (2009).

[50] L.-W. Wang and A. Zunger, Linear combination of bulk bands method for large-scale electronic structure calculations on strained nanostructures, Phys. Rev. B **59**, 15806 (1999).

[51] A. Franceschetti, H. Fu, L.-W. Wang, and A. Zunger, Many-body pseudopotential theory of excitons in InP and CdSe quantum dots, Phys. Rev. B **60**, 1819 (1999).

[52] G. Bester, S. Nair, and A. Zunger, Pseudopotential calculation of the excitonic fine structure of million-atom self-assembled $In_{1-x}Ga_xAs$/GaAs quantum dots, Phys. Rev. B **67**, 161306(R) (2003).

[53] J. B. Foresman, M. Head-Gordon, J. A. Pople, and M. J. Frisch, Toward a systematic molecular orbital theory for excited states, J. Phys. Chem. **96**, 135 (1992).

[54] R. Resta, Thomas-Fermi dielectric screening in semiconductors, Phys. Rev. B **16**, 2717 (1977).

[55] G. A. Narvaez, G. Bester, and A. Zunger, Excitons, biexcitons, and trions in self-assembled (In,Ga)As/GaAs quantum dots: Recombination energies, polarization, and radiative lifetimes versus dot height, Phys. Rev. B **72**, 245318 (2005).

[56] G. A. Narvaez, G. Bester, A. Franceschetti, and A. Zunger, Excitonic exchange effects on the radiative decay time of monoexcitons and biexcitons in quantum dots, Phys. Rev. B **74**, 205422 (2006).

[57] G. Bester and A. Zunger, Cylindrically shaped zinc-blende semiconductor quantum dots do not have cylindrical symmetry: Atomistic symmetry, atomic relaxation, and piezoelectric effects, Phys. Rev. B **71**, 045318 (2005).